The Thesis Committee for Saud Abdulziz Alquwizani
Certifies that this is the approved version of the following thesis:

Three-dimensional Elasto-plastic Modeling of Wellbore and Perforation Stability in Poorly Consolidated Sands

APPROVED BY
SUPERVISING COMMITTEE:

Supervisor:

Mukul M. Sharma

Maša Prodanović

Three-dimensional Elasto-plastic Modeling of Wellbore and Perforation Stability in Poorly Consolidated Sands

by

Saud Abdulziz Alquwizani, B.S.

Thesis

Presented to the Faculty of the Graduate School of

The University of Texas at Austin

in Partial Fulfillment

of the Requirements

for the Degree of

Master of Science in Engineering

The University of Texas at Austin

August 2013

Acknowledgements

My deepest thanks go to Dr. Mukul Sharma for giving me the opportunity to work on such a remarkable research project. My experience with him was nothing but extraordinary; his exemplary support was truly unmatched. I would like to thank Dr. Maša Prodanović for her insights and suggestions for my thesis. Special thanks go to Sung Hyun Kim for all the effort he put in helping me with the simulation coding; his previous work has paved the way for me to accomplish this research.

I would also like to thank everyone involved at the Hydraulic Fracturing and Sand Control JIP. I thank Jin Lee for all her efforts in making my research at the University of Texas Austin a pleasant experience. I would like also to thank my officemates Somnath Mondal and Lionel Ribeiro for all their help during my research and the writing of my thesis. I also thank Ripudaman Manchanda for his help with FLAC3D. I thank all my college friends from the Colorado School of Mines for their friendship and support throughout the years. My thanks go also to Mohammed Salamah for his support and encouragement during my studies at UT.

My appreciation goes to Saudi Aramco for giving me the opportunity to pursue this degree and to all my work colleagues who made it possible.

Last but not least, I thank my parents and my sisters for their continuous support and encouragement all through my educational life.

Abstract

Three-dimensional Elasto-plastic Modeling of Wellbore and Perforation Stability in Poorly Consolidated Sands

Saud Abdulziz Alquwizani, M.S.E.

The University of Texas at Austin, 2013

Supervisor: Mukul M. Sharma

A three-dimensional numerical model was developed to simulate the stability of wellbores and perforations in poorly consolidated sandstone formations. The model integrates the post-yield plastic behavior of granular materials in order to investigate the mechanical instabilities associated with wellbores completed in such formations. Fluid flow and poroelastic stresses are computationally coupled with mechanical calculations to generate pore pressure and stress distribution in the sand. The sand erosion model developed by Kim (2010) is adopted to predict the rate of sand production based on the proposed erosion criterion.

It has been widely reported in the literature that sanding can be greatly influenced by in-situ stress anisotropy, completion geometry, wellbore placement, and perforation orientation. Through advanced modeling and meshing techniques, the model developed in this thesis is capable of simulating complex completion configurations and operational conditions for the purpose of researching the impact of these factors on the wellbore and perforation stability. Accordingly, the model

can be utilized to design a completion that minimizes sand production and optimizes the mechanical stability of the wellbore for a specific in-situ state of stress.

Results obtained from the model show that vertical wellbores produce less sand compared to horizontal wellbores in the case where the overburden stress is the maximum in-situ stress. In addition, orienting the perforation in the direction with the least plastic strain development results in a more stable perforation tunnel with less sand production. Therefore, in a horizontal wellbore, vertically oriented perforations are more stable than horizontally oriented perforations and can withstand higher drawdown pressure before sand is produced. The model was extended to simulate the impact of mechanical and hydraulic interference from adjacent perforations on the evolution of plastic strain. Results from simulation runs show that the perforation spacing has an influence on both the magnitude and the spatial spread of the plastic strain. The model combines the effect of the wellbore diameter, shot density, and the phasing angle to determine the completion configuration with the least sanding risk.

Table of Contents

List of Tables

List of Figures

Chapter 1: Introduction

The production of sand from oil and gas wells has been a costly problem facing the petroleum industry throughout its history. Damage to surface facilities and downhole equipment, in addition to deteriorations to wellbore integrity, all have been encountered as consequences of sand production. Initially, many sand control techniques that were commonly deployed in water wells were adopted by petroleum engineers to limit the severity of sand production (Tausch and Corley 1958). Today, a wide variety of sand control methods are available with various levels of complexity and applicability. Some of these methods include sand screens, gravel packs, frac-packs, and chemical sand consolidation. It has also been shown through field experience that several completion and production strategies can play an important role in limiting sand production.

Some operators elect to allow sand to be produced to the surface at a tolerable rate in accordance with a sand management strategy. This method, if applied successfully, can lead to an increase in oil production rate while reducing capital cost by avoiding the installation of sand control equipment. Understanding the different completion and production parameters that will induce sanding and the degree of their influence is of a great value in selecting the optimal sand handling strategy.

Sand production normally occurs in wells drilled in sandstone formations that are characterized by low mechanical strength. These sands experience a distinct ductile behavior that has been shown to be of a great importance in understanding their mechanical stability. A completion design that results in a

higher mechanical stability results in less sanding risk and ensures the effectiveness of the sand control equipment.

The objective of the research is to construct a model capable of simulating mechanical instabilities of wellbore completions in poorly consolidated sands that could readily be used for real field applications. The model needs to provide tangible insights on how to reach an optimum completion design that minimizes the sanding risk associated with such instabilities.

1.1 MODEL OVERVIEW

Sand production from oil and gas wells is a complex process controlled by a large number of factors. Many of these factors are interrelated and subject to change over the life of the well. Therefore, this research aims to construct a computationally efficient simulator that is able to capture the effect of a wide variety of parameters. Table 1.1 summarizes the simulation parameters integrated in the model.

Table 1.1: Simulation parameters in the model

Mechanical properties	Friction angle, dilation angle, cohesion, hardening/softening regime, elastic moduli, tensile strength
Rock properties	Porosity, permeability, density
Fluid properties	Viscosity, fluid density, compressibility
Boundary conditions	Anisotropic in-situ stresses, reservoir pressure, wellbore pressure
Completion geometry	Wellbore radius, perforation radius, perforation length, perforation density, phasing angle, wellbore inclination, wellbore azimuth, perforation orientation

The model presented in this thesis couples mechanical and fluid flow calculations to provide a solution for stress and pore pressure distribution. For the mechanical behavior, a Mohr-Coulomb material with strain hardening/softening is assumed. Mechanical instability is assumed to be a function of the degree of plastic strain development around the tunnel cavity. The sand erosion formulations developed by Kim (2010), Kim et al. (2011), and Kim and Sharma (2012) are implemented to compute the rate of sand produced from the mechanically failed zones. The sanding criterion followed in this work is able to predict the sand production into the open-hole or the perforation cavity, but it does not compute the portion of this sand that is being transported to surface.

A three-dimensional stress transformation based on the wellbore azimuth, inclination, and perforation orientation is performed in order to study the effect of the wellbore configuration on sanding. In addition, a wellbore model with multiple perforations is constructed to investigate the mechanical interaction between neighboring perforations and how it influences the overall completion stability.

1.2 THESIS OUTLINE

The organization of this thesis follows the same order taken to construct the model. Following this chapter, the second chapter reviews the major work published concerning the modeling of wellbore stability and sand production. It also reviews several experimental and field studies that investigate the effect of completion geometrical configuration on sand production. The third chapter gives an overview of the elasto-plastic formulations that were adopted in the presented model. It also covers different methodologies that researchers undertook to describe the plastic regime of granular materials. The fourth chapter demonstrates how in-situ earth stresses are applied as boundary conditions to the model. Stress distribution generated from the numerical model is successfully validated with analytical solutions for elastic porous media. Also, it explains how stress transformation was performed in order to simulate inclined wellbores and oriented perforations. The fifth chapter describes the structure of the numerical model and its major computational steps. The different geometrical models simulated in the model are also presented. Finally, the sixth chapter provides some concluding remarks based on the results obtained from the model with some emphasis on the effect of configuration of the wellbore completion on sand production.

Chapter 2: Literature Review

Many predictive models were developed in the past to determine the possibility of sand production and to quantify its rate from oil and gas wells. This chapter reviews the available literature concerning the different sand production models and theories. In addition, it summarizes the factors controlling the process of sand failure and the magnitude of their impact on sand production.

Predictive sand production models are generally classified as either analytical or numerical models. Analytical models are mainly used for simplified mechanical behavior and wellbore geometries and might be able to estimate the onset of sand production within an acceptable range. On the other hand, numerical models are used for more complicated analyses with the purpose of computing sanding rates and simulating complex geometries.

The sand production mechanism is primarily controlled by the inherent strength of the rock and the state of stress surrounding the wellbore. Different wellbore configurations result in different stress and pressure distributions in the sand matrix. Hence, this chapter also reviews several observations from experimental, field, and numerical studies that show the effect of wellbore configuration on sand production. In addition, some of the major analytical models and equations that describe the state of stress around wellbores are presented.

2.1 Sand Production Models

Several attempts have been made to understand sand production from oil and gas wells. Some of the early research attributes sand production to the instability of the formation around wellbores due to a mechanical failure of the sand structure. Hall and Harrisberger (1970) suggested that sand production occurs

because of the failure of the sand to form a stable sand arch. The arch was defined as "a curved structure spanning an opening, serving to support a load by resolving the vertical stress into horizontal stresses". They conducted several triaxial tests on unconsolidated sand samples to investigate the conditions in which a stable sand arch would form. They concluded that dilatancy and cohesiveness were required conditions for the stability of a sand arch. They also observed that the outflow of the wetting phase caused a failure of the sand arch. More detailed experimental studies were conducted by Tippie and Kohlhaas (1973), who measured critical flow rates in which the sand arch would lose its stability. They observed a growth in arch size with an increase in flow rate. As the size of the arch grows, it becomes less stable until it fails. After failure, new arches may form again, but they are usually larger and tend to fail at a lower flow velocity as compared to the previous arch. Cleary et al. (1979) observed that confining stress was also an important factor in the size and stability of sand arches. In their experiments, sand-free production rates occur through stable sand arches forming under stress. Also, they observed that the arch size decreases with higher confining stress, resulting in greater stability.

Bratli and Risnes (1981) developed a theoretical model supported by experimental studies to analyze stresses in sand arches and established a criterion for their stability. The authors considered a hemispherical shell of porous material to model sand arching. The material is assumed to behave elastically until it yields according to a Coulomb failure criterion. Consequently, the shell will consist of an inner zone where the material has failed (Coulomb zone) and an outer zone where it still follows an elastic behavior. The suggested stability criterion according to their model is

$$\frac{\mu q}{4\pi k r_1} = \frac{T+1}{T} 4 S_{co} \tan \alpha \tag{2.1}$$

where q is flow rate, μ is the fluid viscosity, k is the permeability, r_1 is the radius of the inner surface, S_{co} is the cohesive strength, α is the failure angle, and T is a constant that depends on the failure angle such that

$$T = 2(\tan^2 \alpha - 1) \tag{2.2}$$

According to this criterion, if the left-hand term exceeds the right-hand term, the Coulomb zone will extend through the entire system causing a total collapse of the sand arch. The authors also proposed another failure mechanism that takes place when the fluid pressure exceeds the radial stress by a value equal to the uniaxial tensile strength. After some mathematical manipulation, this stability criterion reduces to the following formula (where r_s is the radius of the new arch at shell collapse):

$$\frac{\mu q}{4\pi k r_1} = \frac{T+1}{T} 4 S_{co} \tan \alpha \frac{1}{1 + \frac{1}{T}\left(\frac{r_1}{r_s}\right)^{T+1}} \tag{2.3}$$

It is suggested that if the following condition holds for the uniaxial tensile strength, σ_t, the second mode of failure occurs first, otherwise only total collapse is possible as by the first formula specified in Equation 2.1.

$$\sigma_t < \frac{4 S_{co} \tan \alpha}{T} \tag{2.4}$$

Other researchers attempted to predict sand production through some other field methods such as well logs. Stein and Hilchie (1972) proposed to estimate the formation strength by computing the sand elastic moduli from the velocities of acoustic shear and compressional waves obtained from sonic logs. They suggested

that the critical drawdown for the onset of sand production, Δp_c, would be proportionately greater for stronger formation. They suggested the rock shear modulus, E_s, as a parameter to represent the formation strength:

$$\Delta p_c \propto E_s \tag{2.5}$$

So, if the critical drawdown is known for a test zone, T, it is possible to estimate the critical drawdown in another interest zone, Z, within the same formation by knowing the dynamic shear modulus through the equation:

$$(\Delta p_c)_Z = (\Delta p_c)_T \frac{(E_s)_Z}{(E_s)_T} \tag{2.6}$$

Tixier et al. (1975) created a comprehensive method to estimate the formation strength and elastic constants from mechanical property logs, namely sonic and density logs. Through an experimental testing program, it was shown that the ratio of shear modulus to bulk compressibility, G/c_b, can be used as the threshold criterion for sanding in oil or gas reservoirs. Also, it was observed in their experiments that values of G/c_b above $0.8 \times 10^{12} psi^2$ resulted in sand-free production.

Another sanding study was conducted by Veeken et al. (1991) in which they developed simple predictive models based on experimental observations. Sand failure was related to the collapse pressure of hollow cylinder core samples, σ_{TWC}, obtained from thick-wall cylinder (TWC) tests which suggest that

$$\sigma_{v,w} = 0.86 * \sigma_{TWC} \tag{2.7}$$

$\sigma_{v,w}$ is the maximum near-wellbore vertical effective stress, which can be calculated as,

$$\sigma_{v,w} = \sigma_v + \Delta p_{dd} \tag{2.8}$$

Also, the authors observed the following relationship between the critical drawdown pressure and the unconfined compressive strength, σ_{ucs}, which can be used as a conservative sanding prediction

$$\Delta p_{dd} = 0.5 * \sigma_{ucs} \tag{2.9}$$

Morita et al. (1989a) developed an analytical model that assumes that rocks deform and fail according to a Mohr-Coulomb yield surface with linear work-hardening stress-strains in which both shear and tensile failures are possible. Using this method, cavity-failure envelopes were developed that relate well pressure, ΔP_w, with the normalized pressure gradient, G_{PN}. The normalized pressure gradient depends on flow rate, permeability, relative permeability, viscosity and water saturation. The failure envelope changes depending on the stresses, wellbore geometry, and the rock strength; Figure 2.1 shows a typical failure envelope.

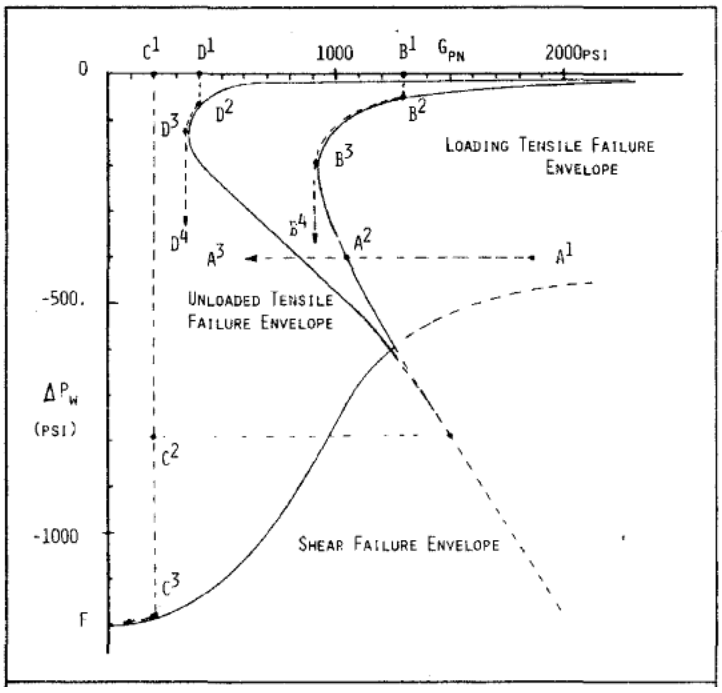

Figure 2.1: Typical perforation cavity-failure envelope (Morita et al. 1989a). Points A-D are some typical flow paths normally encountered during well operations.

Bradford and Cook (1994) developed a semi-analytic elasto-plastic model to predict the onset of sand failure in wellbores. The plastic behavior is modeled using a non-associated Mohr-Coulomb strain hardening deformation theory. In their model, they solved for the stress distribution in both the interior plastic zone forming around the wellbore and the exterior elastic zone. Failure initiation takes place when the borehole wall reaches its peak strength at the end of the hardening region, which corresponds to point B in Figure 2.2.

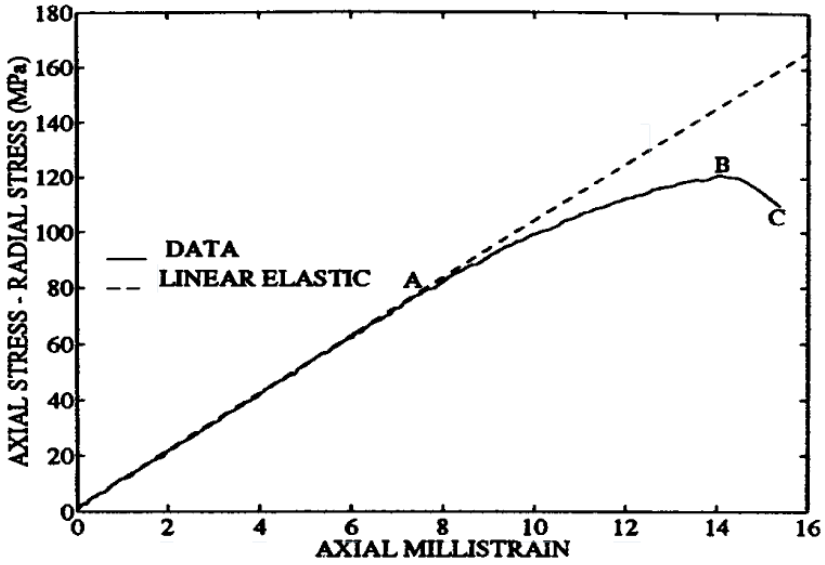

Figure 2.2: Characteristic behavior of soft formations (Bradford and Cook 1994).

With the advancement in computing capabilities, many researchers shifted their effort in modeling sand production to numerical models. Numerical models hold several advantages over analytic models in which they are able to incorporate advanced constitutive physical laws and simulate complex wellbore geometries. Moreover, some of the available numerical models have the capability of estimating the rate of sand production under different conditions; these results are valuable in making key decisions regarding surface facilities design and other sand management requirements.

Generally, there are two approaches to the numerical modeling of sand production: continuum models and discrete element models (Rahmati et al. 2013). The latter utilizes the discrete element method (DEM), which models the behavior of individual sand grains. Although DEM can capture micro-scale phenomena, they are computationally intensive and still not applicable for larger scale field

applications. They also require a detailed knowledge of the rock micro-scale properties, which are not readily available in most cases. Hence, most of the available simulators employ continuum models.

One of the early numerical models was developed by Morita et al. (1989b) to predict the onset of sand production from perforations. This was achieved through two finite element models: a fluid-flow transient model to calculate the pressure distribution and a geostructural model to calculate the stress state and the deformations. Tensile and shear failure envelopes were developed based on a plastic strain limit that depends on rock type. These envelopes are similar to the ones produced by the analytic model developed by Morita et al. (1989a) shown in Figure 2.1.

In a study by van den Hoek et al. (1996), a theoretical predictive sanding model was developed based on bifurcation theory. Contrary to classical continuum models, a Cosserat continuum was used which accounts for the material microstructure and captures the effect of grain size on shear-band thickness. A Mohr-Coulomb constitutive model was used with linearized cohesion hardening and softening. The study was complemented by several sand production experiments performed on hollow cylinder samples of the Castlegate and Saltwash South outcrop sandstones. The study concluded that the type of failure (tensile or shear) only depends on the hole size and the constitutive rock properties. Large cavities, such as boreholes, always fail in shear, while only sufficiently small cavities, such as perforations, can also fail in tension. In this research, experimental studies showed that large cavities failed when a certain threshold value of near-cavity effective stress was reached, independent of the applied drawdown.

Some researchers have argued that sand production is not only caused by rock failure. In their paper, "Hydro-Mechanical Aspects of Sand Production Problem", Vardoulakis et al. (1996) presented a new model for sand production based on hydrodynamic erosion of sand grains. The authors proposed that sand production is a result of two mechanisms: mechanical instability and hydromechanical instability. In this approach, sand grains are allowed to pass freely through the interconnected void space. Sand grains are treated as a separate phase called the fluidized solid. The generation of the fluidized solid leads to a change in porosity resulting in the following equation as a mass balance for this system:

$$\frac{\partial \varphi}{\partial t} = \frac{\dot{m}}{\rho_s} \tag{2.10}$$

where φ is the porosity, ρ_s is the solid density, and $\dot{m}$ is the net rate of mass generation, which is equal to the difference between rate of mass eroded and deposited

$$\dot{m} = \dot{m}_{er} - \dot{m}_{dep} \tag{2.11}$$

The authors proposed the following constitutive law for the rate of the eroded mass,

$$\dot{m}_{er} = \rho_s \lambda (1 - \varphi) c \|\bar{q}_i\| \tag{2.12}$$

where λ is the sand erosion constant and can be related to the spatial frequency of the potential erosion starter point in the solid skeleton. It is expected to be a function of rock damage if the erosion mechanism is coupled with mechanical failure. c is the transport concentration of the fluidized solid, and $\|\bar{q}_i\|$ is the mixture discharge vector. The rate of mass deposition is

$$\dot{m}_{dep} = \rho_s \lambda (1 - \varphi) \frac{c^2}{c_{cr}} \|\bar{q}_i\| \tag{2.13}$$

c_{cr} is a critical value of c that balances the erosion and deposition process.

Skjærstein et al. (1997) performed fluidized column experiments to study the mobilization mechanisms in sands and to calibrate the erosion model proposed by Vardoulakis et al. (1996). Water was flowed upward through a cylindrical sand column and the density was monitored by an X-ray CT scanner. The authors observed that the density of the sand remains relatively constant up to a certain flow rate. They also observed a rise to an upward propagating density wave as flow rate is increased, with lower density below the wave front. The amplitude of the density wave was related to the change in flow rate.

Papamichos et al. (2001) developed a finite-element model that couples the effects of external stresses, fluid flow, and sand erosion to predict volumetric sand production. Sand erosion was modeled using the same equation (Equation 2.12) proposed by Vardoulakis et al. (1996). In addition, they performed several hollow cylinder sand production experiments on synthetic weak sandstones. They observed that the sanding rate increases with increased external stress and higher flow rates; however, it appears that sanding was unaffected by the rate of increase in flow rate. The best simulation results were obtained with a fully-coupled erosion model. In this model, the erosion constant was a function of the plastic shear strain, and cohesion (or the tension cut-off parameter) in which the yield surface is a function of both plastic shear strain and porosity. Figure 2.3 shows data obtained from sanding tests and the simulation results obtained from the model.

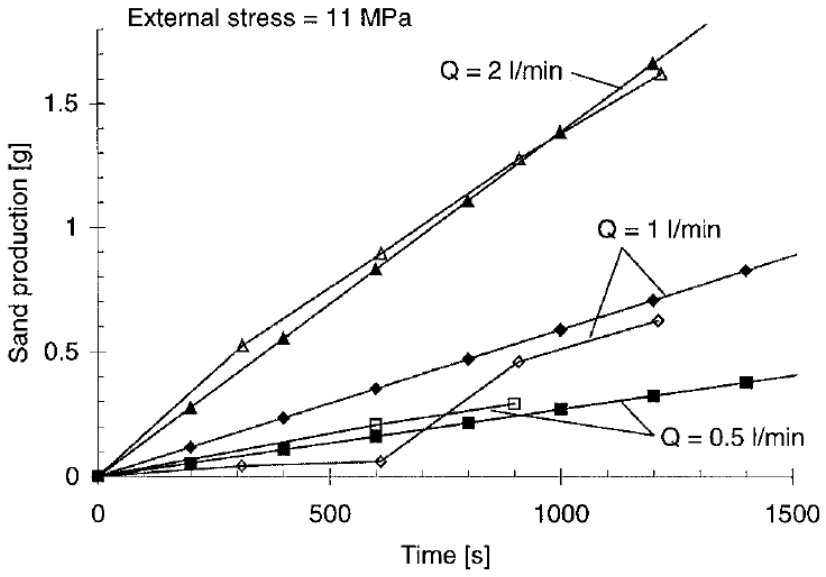

Figure 2.3: Effect of fluid flow rate on sand production. Solid markers correspond to the fully coupled erosion model simulations and hollow markers correspond to test data (Papamichos et al. 2001).

Fjær et al. (2004) developed a simple analytical model based on the erosion principles presented in the numerical model by Papmichos et al. (2001). The model assumes cyclic production of sand as the stiffness of the rock matrix remains constant until the porosity reaches a critical value in which the sand producing zone is produced at once. According to their model, the average rate of sand production, $\dot{M}_s$, from a cylindrical cavity is calculated by,

$$\dot{M}_s = \frac{1}{2}\eta R P_s \left(e^{2\frac{D-D_c}{C_0}} - 1 \right) (Q - S_c q_o) \tag{2.14}$$

where η is the fluid viscosity, R is the cavity radius, D is the drawdown, D_c is the critical drawdown, C_0 is the unconfined strength of the rock, Q is the total flow rate from the cavity, S_c is the surface area of the cavity, q_o is the initial fluid flux, and P_s is defined as,

$$P_s = 4\lambda_s \frac{1-\varphi_o}{\varphi_{cr}^4 - \varphi_0^4} \tag{2.15}$$

where λ_s is the proportionality constant, φ_o is the initial porosity, and φ_{cr} is the critical porosity. The authors proposed that the parameters φ_o and φ_{cr} need to be determined by calibration in a sand production test. The critical drawdown is calculated based on the degree of plastic deformation that will initiate sand production, which determines the extent of the sand producing zone. The authors acknowledged the fact that this model might not be entirely realistic since it predicts that the entire sand producing zone collapses simultaneously. However, experimental studies and numerical simulations based on the discrete element method (DEM) showed that sand is being produced in distinct events as large fragments from the cavity wall. The model also predicts that the probability of producing larger breakouts increases with higher drawdown pressures.

Wan et al. (2003) proposed a sand erosion model in which the sand erosion is governed by Equation 2.12, but it can only be triggered if the fluid velocity exceeds a critical value. The erosion parameter, λ, was related to the accumulated plastic strain, γ^p, through the relationship

$$\lambda = \lambda_o + \frac{\gamma^p}{\alpha + \beta\gamma^p} \tag{2.16}$$

where α and β are constants, and λ_o is the threshold strength above which erosion becomes prevalent. Internal damage due to degradation during the erosion process was modeled through cohesion, C, and friction angle, ϕ, assuming the following relationships

$$C = C_o \frac{\varphi_{max} - \varphi}{\varphi_{max} - \varphi_o} \tag{2.17}$$

$$\phi = \phi_o \frac{\varphi_{max} - \varphi}{\varphi_{max} - \varphi_o} \tag{2.18}$$

in which C_o is the initial cohesion and ϕ_o is the initial friction angle; φ, φ_{max}, and φ_o are the porosity, maximum porosity, and initial porosity, respectively. Figure 2.4 shows the increase in porosity in a simulated sand cavity due to the erosion process after a certain time period.

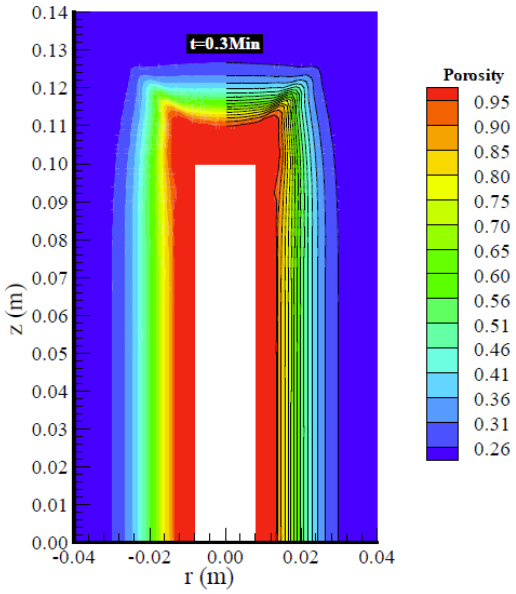

Figure 2.4: Simulated porosity profile in a sand cavity due to erosion at time t=0.3 minutes (Wan et al. 2003).

Vaziri et al. (2002) presented a sand prediction study performed on deep, HPHT wells in which several analytical and numerical approaches are examined. The analytical model distinguishes between shear and tensile failure. For shear failure, the sanding criterion for a vertical, cased and perforated well is

$$CBHFP \geq = \frac{3\sigma_1 - \sigma_2 - \sigma_y}{2 - A} - P_r \frac{A}{2 - A} \tag{2.19}$$

where CBHFP is the critical bottom-hole flowing pressure, σ_1 and σ_2 are the total principal major and minor stresses, σ_y is the formation strength, and A is the poroelastic constant:

$$A = \frac{(1-2\nu)\alpha}{1-\nu} \tag{2.20}$$

where ν is Poisson's ratio and α is Biot's constant. The formation strength can be approximated from thick-wall cylinder testes:

$$\sigma_y = \lambda \times TWC \tag{2.21}$$

where λ is a factor depending on the ratio of outside diameter to inside diameter of the sample. For tensile failure, the critical drawdown pressure (CDP) for liquids can be calculated using the equation:

$$CDP = \frac{4\ C\ cos\ \phi}{1-sin\ \phi} \tag{2.22}$$

where C is the cohesion and ϕ is the friction angle. The results obtained by analytical methods have been shown to be overly restrictive and underestimate the sand stability when compared to field observations. Therefore, the authors proposed an elasto-plastic finite element model that fully couples fluid flow and stress calculations to analyze sanding. The model simulates the response of reservoir material to different conditions by adjusting the strength parameters, which results in multi-variant failure envelopes. For example, cohesive strength is reduced after shearing or water breakthrough to simulate the weakening for the rock matrix. Figure 2.5 shows a graphical representation of this process.

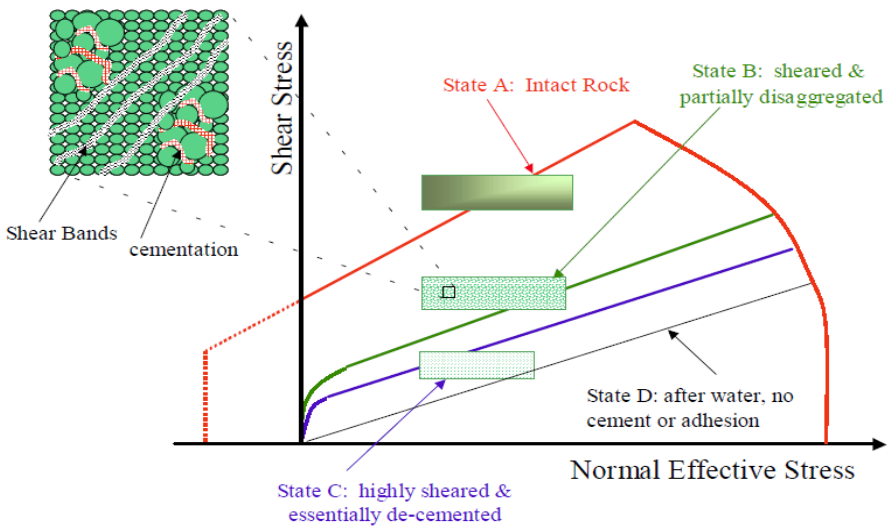

Figure 2.5: Transformation of the reservoir material from intact to broken up state (Vaziri et al. 2002).

Nouri et al. (2004) developed a 2D finite-difference model with a bilinear strain hardening/softening Mohr-Coulomb yield criterion to model the rock elasto-plastic behavior. They assumed that sanding occurs if the exposed rock fails under tension or if a shear-failed rock falls into tension. Their model achieved remarkable results in simulating sand production experiments from hollow synthetic sand samples.

Detournay et al. (2006) developed a 2D finite-difference hydro-mechanical model to simulate sand erosion. The model assumes a strain-softening Mohr-Coulomb material where yielding is a pre-requisite to sand production. Sanding occurs at the cavity-boundary layer when a local fluid pressure gradient is higher than a local stress-dependent critical value. This critical stress value is a function of grain size. For Darcy flow, the critical stress value can be expressed by the critical specific discharge vector, q_{cr}:

$$q_{cr} = a\frac{k(1-\varphi)}{R_p}(C_r - \sigma_t' \tan\phi_r) \tag{2.23}$$

where a is a dimensionless coefficient, k is the permeability, R_p is the radius of one sand particle, φ is the porosity, C_r is the residual cohesion, ϕ_r is the residual friction angle, and σ_t' is the normal bulk effective stress acting parallel to the boundary, which is compressive for the above equation. In case it is a tensile stress,

$$q_{cr} = 0 \tag{2.24}$$

Based on the critical discharge vector, the condition for sand production is

$$q_u > q_{cr} \tag{2.25}$$

q_u is the specific discharge component in the direction of the exterior normal. When sand production starts, porosity increases until it reaches a critical value, which causes the sand to collapse. Any collapsed section in the boundary layer is produced at once and is removed from the model. The rate of sand production is being modeled similar to the proposed equation (Equation 1.12) by Vardoulakis et al. (1996):

$$\frac{dm_s}{dt} = \rho_s \lambda(1-\varphi)(q_u - q_{cr}) \tag{2.26}$$

where m_s is the mass of sand produced, λ is a dimensionless parameter.

Chin and Ramos (2002) proposed a new sanding model for weak reservoirs. The model is a single-phase, fully coupled model that predicts volumetric sand production rate for both 2D and 3D problem. It assumes that the amount of sand production is directly related to the volumetric plastic strain around the wellbore. The Drucker-Prager elasto-plastic model was selected as a constitutive model in which its shear failure envelope is internally tangential to the Mohr-Coulomb yield surface. The model provides fluid pressure, displacements, strain, and stress distribution as a function of time. Sand production is calculated based on the

incremental change in the volumetric plastic strain at each time step based on the equation,

$$V_{n+1} = V_n + \sum_{m=1}^{nel} \left(\Delta\varepsilon_v^p/\varphi\right)_{m,n+1}.\Omega_m \tag{2.27}$$

where V_{n+1} is the cumulative bulk volume of sand produced at t_{n+1}, V_n is the cumulative bulk volume of sand produced at t_n, n is the time step index, $\Delta\varepsilon_v^p$ is the incremental plastic strain of an element between t_{n+1} and t_n, m is the element index, Ω_m is the volume of element m, and nel is the total number of elements around the wellbore region. The model was verified by four sanding experiments performed on outcrop specimens of Salt Wash South sandstone formation. Figure 2.6 shows the results for their first test.

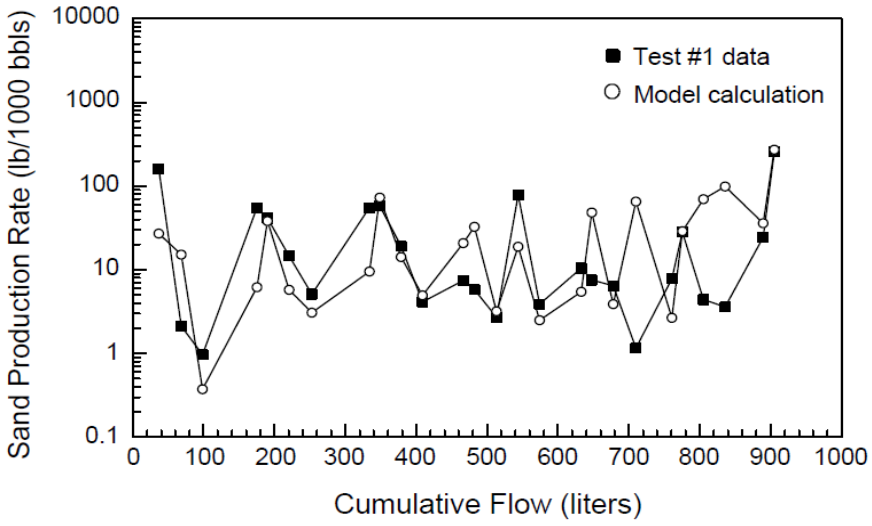

Figure 2.6: Comparison of calculated and measured sand production for Test#1 (Chin and Ramos 2002).

Based on simulation results, the authors identified two sanding processes: early drawdown induced sanding and depletion induced sanding. In the first period,

sand production will diminish after a few days to a few weeks until the pore pressure around the wellbore has stabilized. For the second period, the reservoir pressure decline results in a change of state of stress leading to shear-failure induced sanding. The authors discussed the effect of rock strength, flow rate, and fluid viscosity in both sanding processes. Figure 2.7 shows an example of the simulation results during the early drawdown period.

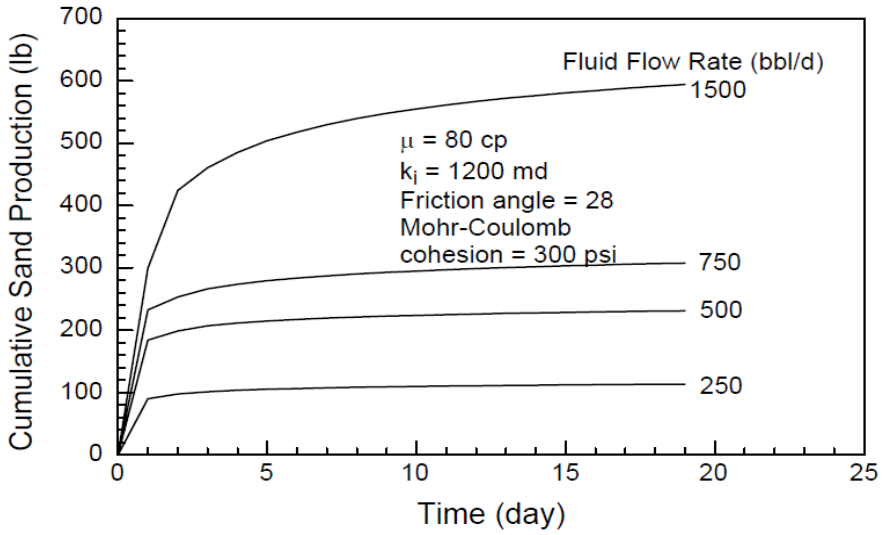

Figure 2.7: Simulation results showing the effect of fluid flow rate on cumulative sand production in the early drawdown period (Chin and Ramos 2002).

It is worth mentioning that since many of the erosion models assume a reduction in porosity as a sand erosion mechanism, most of them re-adjust permeability values based on the Carman-Kozeny relationship in which k_o is the initial permeability

$$k = k_o \frac{\varphi^3}{1-\varphi^2} \tag{2.28}$$

Kim (2010) developed a 3D finite-difference model assuming a strain-softening Mohr-Coulomb material in which yielding is a pre-requisite of sand

production. A sanding criterion was proposed based on force balance calculations performed on each cavity-exposed grid-block that failed in either tension or shear. The author suggested that for sanding to occur the sand must fail and the following criterion must be satisfied to sand sand erosion,

$$F_f > F_r \tag{2.29}$$

where F_f is the hydrodynamic force that acts parallel to the flow and is generated by the pore pressure difference between the inner and exposed faces of the grid, and F_r is the resistance force due to friction. These forces are calculated as follows,

$$\begin{aligned} F_r = {} & A_r\sigma_r|_{r=L}^{r=0} - A_\theta\sigma_{\theta r}|_{r=0}^{\theta=L} - A_z\sigma_{zr}|_{z=0}^{z=L} + \mu_f(A_\theta\sigma_\theta|_{\theta=0} + A_\theta\sigma_\theta|_{\theta=L} \\ & + A_z\sigma_z|_{z=0} + A_z\sigma_z|_{z=L}) \end{aligned} \tag{2.30}$$

$$F_f = A_r p|_{r=L} - A_r|_{r=0}\, p_w \tag{2.31}$$

where A is the area of grid-block normal to the direction of subscript, σ is the stress, p is pore pressure, and p_w is the pressure on the open face which is equivalent to the wellbore pressure. A positive hydrodynamic force indicates the force acting in the direction of flow. Figure 2.8 shows a diagram of the stresses on a grid-block.

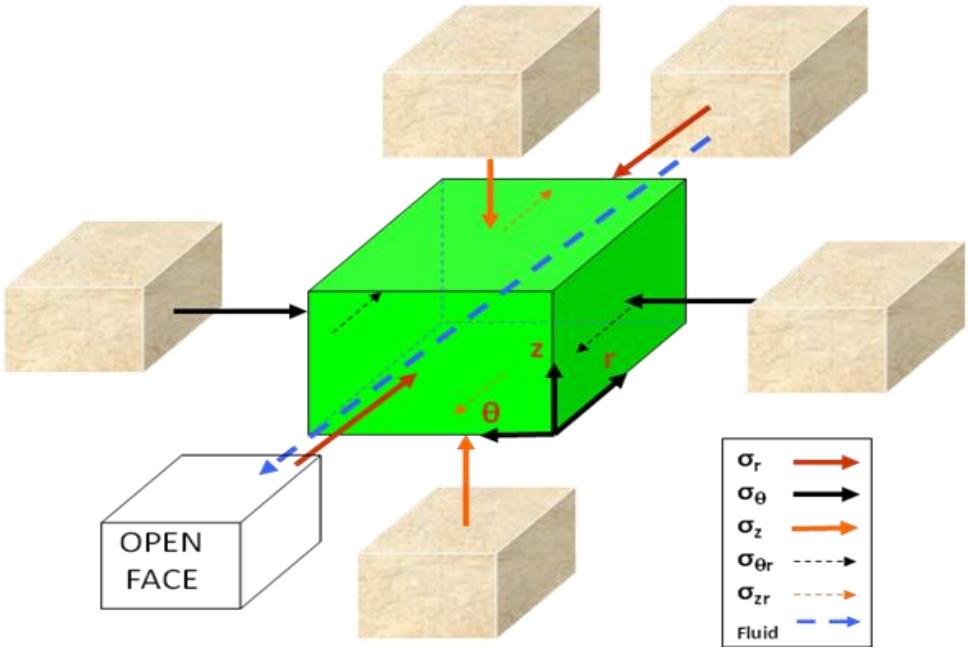

Figure 2.8: Stresses acting on a grid-block with one open face (Kim 2010).

The mass of produced sand is calculated based on the density, porosity, and the grid-block volume, V_z:

$$m_s = \rho_s V_z \varphi \tag{2.32}$$

In this model, cohesion was reduced as a result of increasing water cut in order to simulate the effect of two-phase flow on sand production. The model was successful in matching the sanding profiles in several experimental studies from the literature. Excellent simulation results were achieved by the model when the post-failure behavior of the material was known. Figure 2.9 demonstrates one of these simulation in which the sand production rate was computed as a function of the axial stress in a sanding experiment.

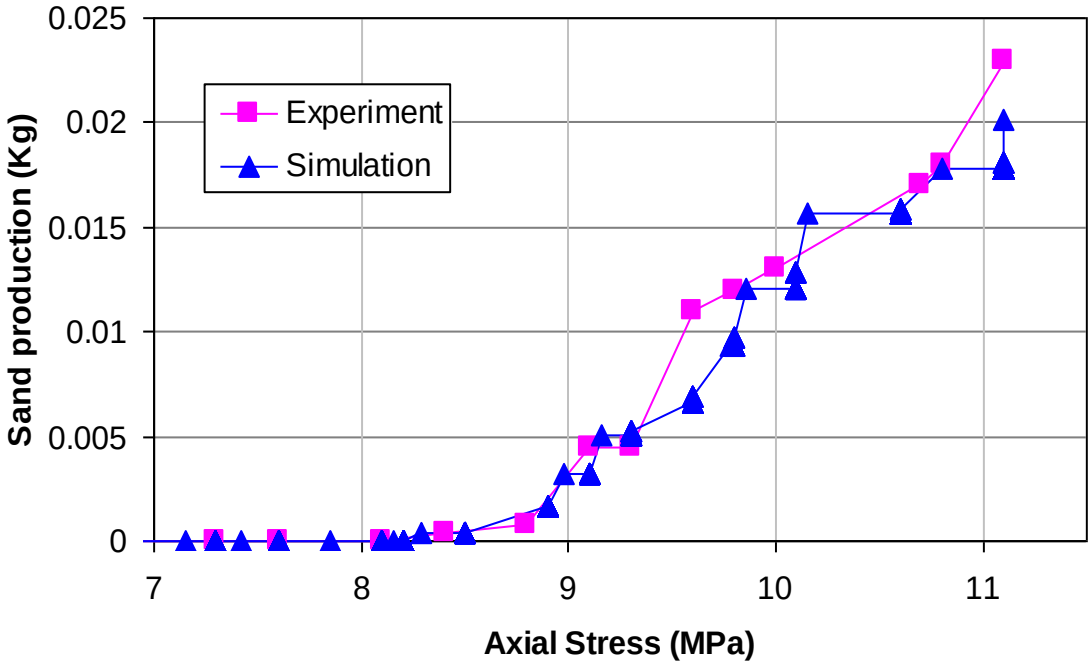

Figure 2.9: Sand production profile from experiment and simulation for varying axial stress (Kim 2010).

2.2 The Effect of Wellbore and Perforation Geometry on Sand Production

It has been reported from both experimental and field observations that the geometry and orientation relative to principle stresses have a considerable effect on sanding from wellbores and perforation tunnels. There is a considerable amount of literature that investigates factors affecting sand production by means of experimental, field, and numerical studies.

Vriezen et al. (1975) suggested that the stability of a perforation is a function of its geometry, mechanical strength, and the effective stress distribution in the vicinity of the perforation. However, fluid flow into and through the perforation causes an erosive action that increases its diameter, and consequently, reduces it mechanical stability. A series of 27 perforation-erosion experiments were carried out on stressed samples from Groningen gas field cores. The experimental settings were designed to study the effect of both axial and radial flow on sand erosion. The authors observed that the onset of continuous erosion is primarily controlled by the effective radial load. For weakly cemented sandstone, the variation in perforation diameter and the addition of a radial flow to the axial flow did not have a significant influence on the onset of continuous erosion. Finally, it was observed that at a constant load, the repeated variations in gas flow velocity below a level at which erosion stopped did not induce additional sand production.

Experiments on large blocks of Castlegate sandstone were conducted to evaluate sanding tendencies (Koojiman et al. 1992; Behrmann et al. 1997). The blocks were 0.7mx0.7mx0.8m in size saturated with oil at a residual saturation of 3% KCL brine. A 4" wellbore was drilled, cased, cemented, and then perforated at 90^0 phasing. The block was stressed with vertical stress as the maximum principal stress and with unequal horizontal stresses. Several important observations were

made from these tests. In some of the perforations, loose sand formed stable hemispherical arches at the wellbore/tunnel interface, which contributed to reducing the sanding rate. In open perforation tunnels, pressure depletion or excessive drawdown resulted in tunnel failure, which led to sand production. Also, it has been observed that perforation orientation had an effect on sand production rates in which perforations shot in the direction of the minimum horizontal stress had a higher sand production rate as shown in Figure 2.10. It was evident that some sand production was caused by perforation-to-perforation failure. Behrmann et al. (1997) suggested selecting the shot density based on the minimum allowable perf-to-perf distance and the maximum average production rate per perforation. Moreover, it was observed that smaller-diameter perforation tunnels are more stable than larger-diameter tunnels (Behrmann et al. 1997). Finally, introduction of brine flow led to large bursts of sand production; however, it was observed that when the two-phase flow was changed to brine only, sand production stopped (Koojiman et al. 1992).

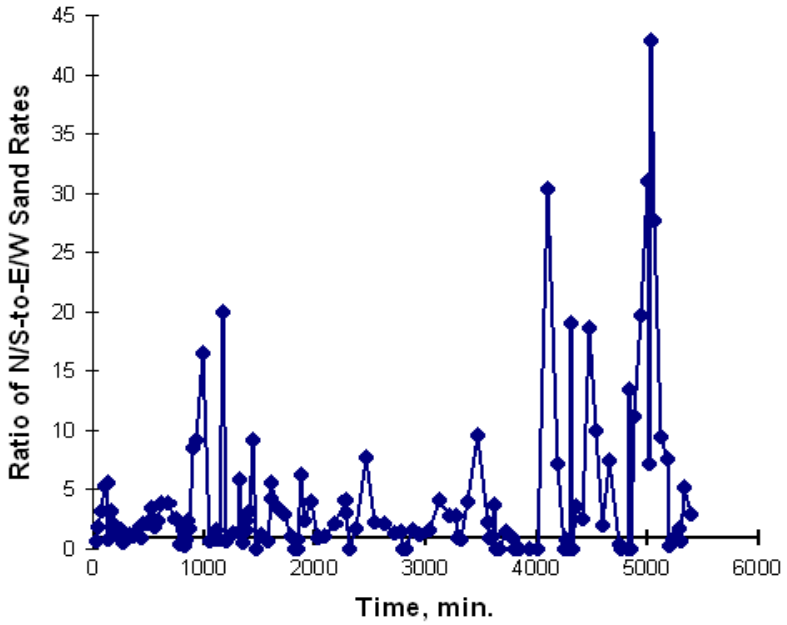

Figure 2.10: Ratio of N/S-to-E/W sand rates. Maximum horizontal stress was in the E/W direction (Behrmann et al. 1997).

Another set of experiments that were conducted on large blocks of artificial sandstone was reported by Kooijman et al. (1996). The objective of this experiment was to study the effect of drawdown, water cut, in-situ stresses, and completion type on sanding from horizontal wellbores. It was observed in open holes that a rise in sand production was observed with an increase in vertical stress until wormholing to the sample boundary caused a termination of the test. Similar results with massive sand production were observed as a result of introducing water flow.

Walton et al. (2001) performed sanding experiments on unconsolidated sands with a porosity of about 36% and permeabilities in the range of 5 to 10 Darcies. The experiments consisted of single-shot perforations in stressed cylindrical samples. Experimental conditions were varied to study the effect of different parameters such as saturation fluids, and flow rate. They observed that the

initial perforation tunnel collapsed upon perforating the samples regardless if they were perforated balanced or underbalanced. Also, fluid flow generated a dilated zone around the tunnel entrance in which its radius increased with flow rate until a critical flow rate was achieved, causing the entire sample to collapse. Finally, a stable arch that grew in size with flow rate was achieved in a brine-kerosene system; however, with a single-phase or OMS/Water system, a stable arch was not achieved. The authors suggest that a relatively high interfacial tension between brine and kerosene contributed to the strength of the material.

In addition to experimental studies, several field studies reported the effect of wellbore geometry on sand production. Morita and McLeod (1995) reported a field study where wells suffered from sanding and casing collapse problems. The reservoir is highly depleted with one horizontal stress significantly higher than the overburden stress. The study reported that three wells were perforated with 180° phasing in the maximum in-situ stress direction. All three wells did not experience casing collapse while two of them experienced substantially reduced sanding problems when compared to the surrounding wells. The study was supported by a numerical study utilizing a finite-element model. It suggested that a sheared zone with reduced strength might form in the direction of the minimum horizontal stress (Figure 2.11). If perforations are shot in this direction, they will produce the disintegrated grains in the sheared zone, which will form a cavity behind the casing, causing it to collapse. The authors consequently suggested that the perforations be shot in the maximum in-situ stress direction. Also, the authors suggested that perforations shot in the well azimuth become very stable with increased well inclination compared with perforations shot perpendicular to well azimuth.

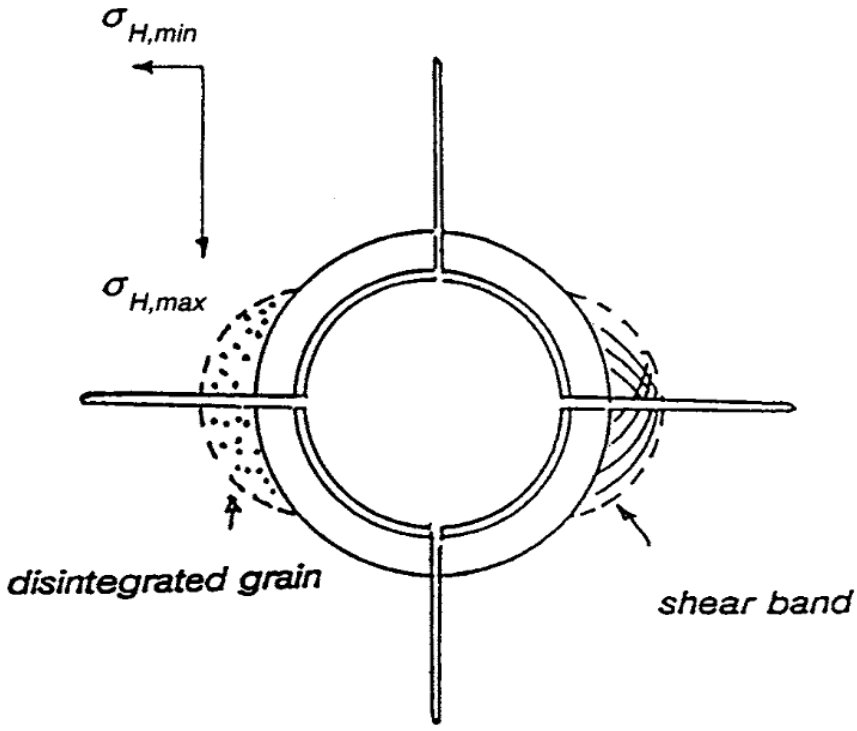

Figure 2.11: Sheared zone around a cased well (Morita and McLeod 1995).

Tronvoll et al. (2004) reported a field case study form the Varg Field in the North Sea. Prior to developing the field, sand production risk was judged "substantial" based on data from appraisal wells. Therefore, most wells were completed with oriented perforations at 180° phasing. Since then, the reservoir has been depleted by more than 1,450 psi with limited sand production. Their recommended strategy for weak sands is to complete the wells with vertically shot, low-density perforations at 180° phasing in horizontal and highly deviated wells.

Sulbaran et al. (1999) reported a case study from a field in Lake Maracaibo, Venezuela where sand production has been a major operational problem. A finite-element model with Mohr-Coulomb elasto-plastic behavior was deployed to determine the optimum perforation orientation. They assumed that sand failure

occurs if the equivalent plastic strain exceeds a critical value determined from triaxial tests. The study concluded that oriented perforations within $\pm 25^0$ from the direction of the maximum horizontal stress will result in stable perforations. Another study was conducted to determine the minimum perforation-to-perforation distance that would prevent rock failure. Using a Mohr-Coulomb yield criterion, they determined that a distance of $3xD_{perf}$ is sufficient to minimize the effect of perforation interference. Four wells were perforated according to the study findings. The reported sand production from all wells was considerably below the field average. Several other field studies (Palmer et al. 2006; Rahman et al. 2010) have also mentioned reduced sanding problems due to optimized perforation and wellbore geometry.

Santarelli et al. (1991) used a 3D finite element code to study the stability of perforations. The authors assumed a homogenous isotropic linear medium. In this parametric study, perforation orientation, perforation density, perforation length, perforation diameter, and cement quality were analyzed to determine their effect on sanding risk. Sand production risk was calculated using the following equation, where $\sigma^{*\prime}_{max}$ is the maximum effective stress around the cavity and σ'_v is the vertical in-situ stress.

$$R = {\sigma^{*\prime}_{max}}/{\sigma'_v} \tag{2.33}$$

They concluded that perforation length had no effect on sand production. Also, perforation entrance hole diameter does not influence sanding as long as perforation density is not too large. For large perforation densities, mechanical interaction between perforation increases sanding risk. Sanding risk due to perforation orientation was studied as a function of the following two ratios, where

σ'_H is the maximum horizontal effective stress and σ'_h is the minimum horizontal effective stress.

$$K'_H = {}^{\sigma'_H}/_{\sigma'_v} \tag{2.34}$$

$$K'_h = {}^{\sigma'_h}/_{\sigma'_v} \tag{2.35}$$

Figure 2.12 shows the findings of the study and the recommended perforation orientation angle, θ, measured from σ'_H for a vertical well.

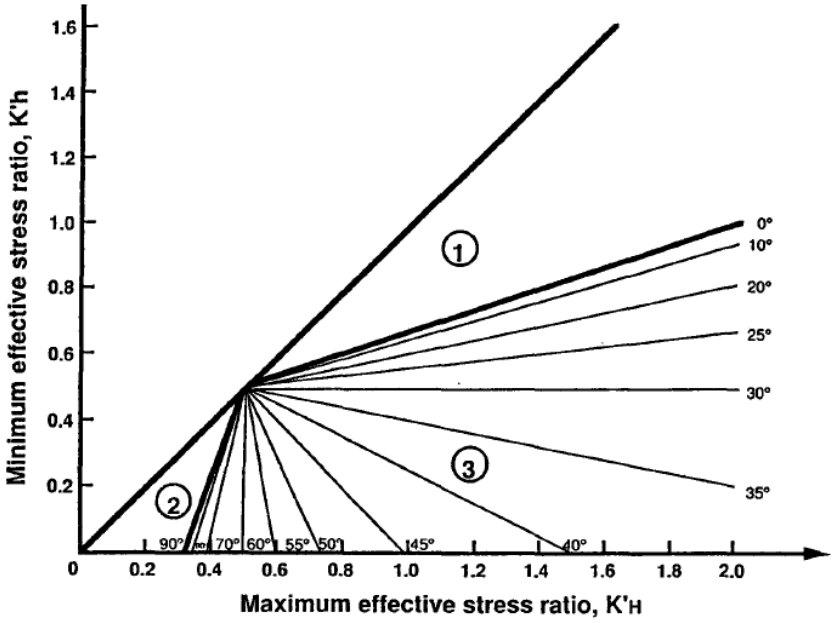

Figure 2.12: Optimal perforation orientation chart. In region 1, perforations should be shot parallel to the maximum horizontal stress. In region 2, perforations should be shot parallel to the minimum horizontal stress (Santarelli et al. 1991).

Venkitaraman et al. (2000) presented three major techniques that could be used to prevent sand production in perforated completions. These techniques are based on field data and supported by a theoretical elasto-plastic model. First, it was recommended to use deep penetrating charges with smaller holes for a higher

stability in a single perforation. Second, perforation spacing should be increased to prevent inter-linking of failed zones around adjacent perforation tunnels. Since reducing the perforation density will result in the undesirable effect of higher flow rate per perforation, increasing the spacing should be achieved by optimizing the perforation phasing. For a given shot density and wellbore radius, optimum perforation phasing is accomplished by having equal spacing between three adjacent perforations (L_1=L_2=L_3) as shown in Figure 2.13.

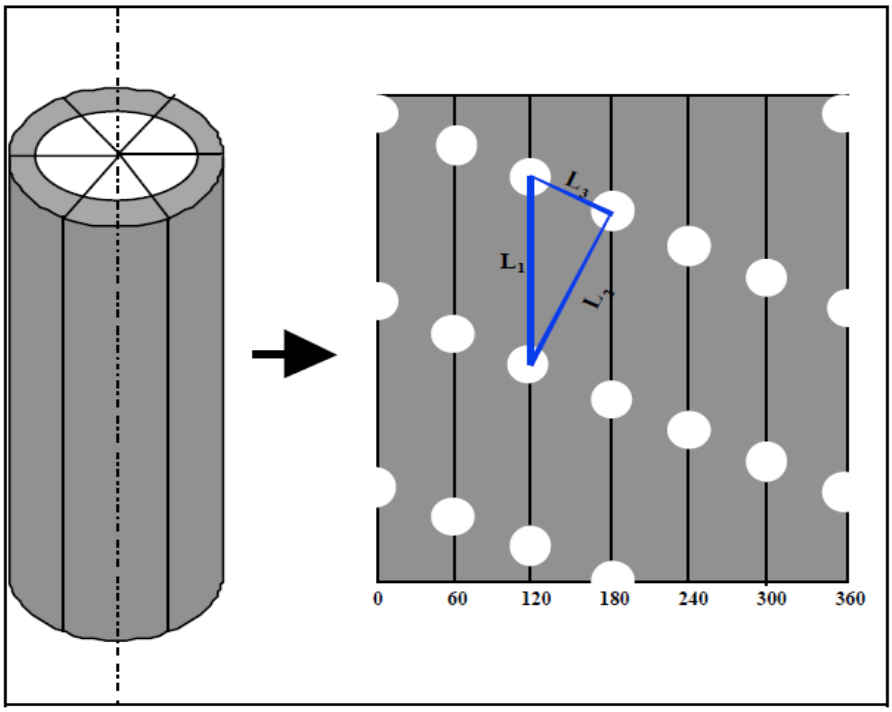

Figure 2.13: Perforations at the wellbore sandface are shown in 2D with the spacing between adjacent perforations (Venkitaraman et al. 2000).

Since this configuration might be not practically possible, the optimum phasing is achieved when any two of these spacings are equal. Figure 2.14 shows the

inter-linking of the failed zone at a perforation phasing of 60^0 and an optimized phasing of 99^0 with the increase in reservoir depletion.

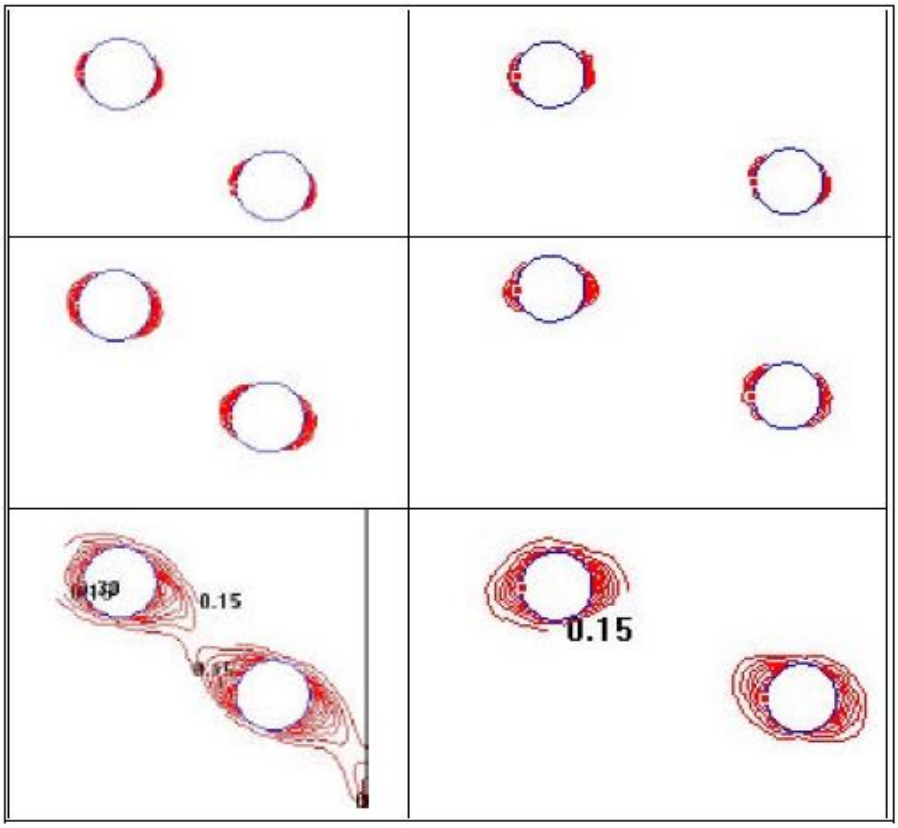

Figure 2.14: Simulation of inter-linking between the failed zones using an elasto-plastic model. Depletion is increased when moving down the column for 60^0 (left) and 99^0 (right) phasing (Venkitaraman et al. 2000).

The third recommended technique is to use oriented perforation where there is a large contrast between in-situ principal stresses. Perforations should be oriented in the direction of maximum stability as identified by the work of Santarelli et al. (1991) summarized earlier. The authors also proposed the use of underbalance perforation to reduce the extent of the crushed zone. The crushed zone is characterized by a reduced permeability resulting in greater pressure drop.

This increase in pressure drop might lead to tensile failure in the sand matrix and subsequent sand production. The authors also recommended selective perforation in wells where the rock strength varies drastically with depth.

2.3 STRESS DISTRIBUTION AROUND WELLBORES

The existence of a wellbore results in a distortion of in-situ stresses that naturally exist in the ground. As shown in the previous sections, stresses are a determinant factor in any sand production model. In this section of the paper, several analytical models that describe the state of stress around wellbores are presented. Although all of these models are developed for simple geometries and use several simplistic assumptions, they are an excellent tool to illustrate the downhole state of stress and can also be used as a validating tool for numerical models. Once these numerical models are validated, they can later be used for more complex geometries.

Hubbert and Willis (1957) proposed the superposition of the Lamé solution for thick-walled cylinders and Kirsch's equations for a hole in an infinite plate in order to calculate the stress distribution around a vertical, perfectly cylindrical wellbore, assuming a linearly elastic, isotropic medium. Lamé equations to calculate the stresses (in cylindrical coordinates with positive compressive stresses) can be expressed as,

$$\sigma_{rr} = \frac{p_o r_o^2 - p_i r_i^2}{r_o^2 - r_i^2} - \frac{r_i^2 r_o^2 (p_o - p_i)}{r_o^2 - r_i^2}\left(\frac{1}{r^2}\right) \tag{2.36}$$

$$\sigma_{\theta\theta} = \frac{p_o r_o^2 - p_i r_i^2}{r_o^2 - r_i^2} + \frac{r_i^2 r_o^2 (p_o - p_i)}{r_o^2 - r_i^2}\left(\frac{1}{r^2}\right) \tag{2.37}$$

$$\tau_{r\theta} = 0 \tag{2.38}$$

Here p_o is the external pressure, p_i is the internal pressure, r_i is the inner radius, r_o is the outer radius, r is the radius at which the stress is calculated (Fjær et al. 2008, 139). Kirsch's equations are expressed in the following form (Jaeger and Cook 1979, 251), where S_H and S_h are the maximum and minimum in-situ principal stresses, respectively, and θ is the angle from S_H:

$$\sigma_{rr} = \frac{1}{2}(S_H + S_h)(1 - \frac{r_i^2}{r^2}) + \frac{1}{2}(S_H - S_h)\left(1 + \frac{3r_i^4}{r^4} - \frac{4r_i^2}{r^2}\right) \quad (2.39)$$

$$\sigma_{\theta\theta} = \frac{1}{2}(S_H + S_h)\left(1 + \frac{r_i^2}{r^2}\right) - \frac{1}{2}(S_H - S_h)\left(1 + \frac{3r_i^4}{r^4}\right)\cos 2\theta \quad (2.40)$$

$$\tau_{r\theta} = \frac{1}{2}(S_H - S_h)\left(1 - \frac{3r_i^4}{r^4} + \frac{2r_i^2}{r^2}\right)\sin 2\theta \quad (2.41)$$

In the case that $r_o \gg r_i$, the superposition of the previous equations in a poroelastic medium with constant pore pressure, p_p, leads to the following equations (Zoback 2010, 170)

$$\sigma_{rr} = \frac{1}{2}\left(S_H + S_h - 2p_p\right)\left(1 - \frac{r_i^2}{r^2}\right) + \frac{1}{2}(S_H - S_h)\left(1 + \frac{3r_i^4}{r^4} - \frac{4r_i^2}{r^2}\right)\cos 2\theta + \frac{\Delta p r_i^2}{r^2} \quad (2.42)$$

$$\sigma_{\theta\theta} = \frac{1}{2}\left(S_H + S_h - 2p_p\right)\left(1 + \frac{r_i^2}{r^2}\right) - \frac{1}{2}(S_H - S_h)\left(1 + \frac{3r_i^4}{r^4}\right)\cos 2\theta - \frac{\Delta p r_i^2}{r^2} \quad (2.43)$$

$$\tau_{r\theta} = \frac{1}{2}(S_H - S_h)\left(1 - \frac{3r_i^4}{r^4} + \frac{2r_i^2}{r^2}\right)\sin 2\theta \quad (2.44)$$

where Δp is the difference between the wellbore pressure and formation pore pressure. The equations above assume a constant pore pressure, but in a producing well, pore pressure distribution will vary and the stress distribution changes accordingly. Risnes et al. (1982) solved for the stress distribution in an isotropic elastic material by using Darcy's law to calculate pore pressure at a constant flow rate.

$$\sigma_{rr} = S_h + (S_h - p_i)\frac{r_i^2}{r_o^2 - r_i^2}\left[1 - \left(\frac{r_o}{r}\right)^2\right] - (p_o - p_i)\frac{1-2\nu}{2(1-\nu)}\alpha\left\{\frac{r_i^2}{r_o^2 - r_i^2}\left[1 - \left(\frac{r_o}{r}\right)^2\right] + \frac{\ln(r_o/r)}{\ln(r_o/r_i)}\right\} \quad (2.45)$$

$$\sigma_{\theta\theta} = S_h + (S_h - p_i)\frac{r_i^2}{r_o^2 - r_i^2}\left[1 + \left(\frac{r_o}{r}\right)^2\right] - (p_o - p_i)\frac{1-2\nu}{2(1-\nu)}\alpha\left\{\frac{r_i^2}{r_o^2 - r_i^2}\left[1 + \left(\frac{r_o}{r}\right)^2\right] + \frac{\ln(r_o/r) - 1}{\ln(r_o/r_i)}\right\} \quad (2.46)$$

$$\sigma_{zz} = S_v + 2\nu(S_h - p_i)\frac{r_i^2}{r_o^2 - r_i^2} - (p_o - p_i)\frac{1-2\nu}{2(1-\nu)}\alpha\left\{\frac{2\nu r_i^2}{r_o^2 - r_i^2} + \frac{2\ln(r_o/r) - \nu}{\ln(r_o/r_i)}\right\} \quad (2.47)$$

where ν is Poisson's ratio and S_v and S_h are the vertical and horizontal stresses, respectively. Assuming a constant reservoir pressure at a drainage r_e that is much larger than the well radius, the equations simplify to (Fjær et al. 2008, 143)

$$\sigma_{rr} = S_h - (S_h - p_i)\left(\frac{r_i}{r}\right)^2 + (p_o - p_i)\frac{1-2\nu}{2(1-\nu)}\alpha\left[\left(\frac{r_i}{r}\right)^2 - \frac{\ln(r_e/r)}{\ln(r_e/r_i)}\right] \quad (2.48)$$

$$\sigma_{\theta\theta} = S_h + (S_h - p_i)\left(\frac{r_i}{r}\right)^2 - (p_o - p_i)\frac{1-2\nu}{2(1-\nu)}\alpha\left[\left(\frac{r_i}{r}\right)^2 + \frac{\ln(r_e/r)}{\ln(r_e/r_i)}\right] \quad (2.49)$$

$$\sigma_{zz} = S_v - (p_o - p_i)\frac{1-2\nu}{2(1-\nu)}\alpha\left[\frac{2\ln(r_e/r) - \nu}{\ln(r_e/r_i)}\right] \quad (2.50)$$

In addition, Risnes et al. (1982) solved for the stress distribution in an isotropic plastic material by using Coulomb failure criterion. In this solution, they assumed a plastic zone forming around the wellbore with an elastic exterior zone.

Bradley (1979) provided a solution for stress distribution around inclined boreholes for an elastic medium as a function of the radial distance away from the wellbore.

$$\sigma_r = \left(\frac{\sigma_x + \sigma_y}{2}\right)\left(1 - \frac{{r_i}^2}{r^2}\right) + \left(\frac{\sigma_x - \sigma_y}{2}\right)\left(1 + \frac{3{r_i}^4}{r^4} - \frac{4{r_i}^2}{r^2}\right)\cos 2\theta + \tau_{xy}\left(1 + \frac{3{r_i}^4}{r^4} - \frac{4{r_i}^2}{r^2}\right)\sin 2\theta + p_i\frac{{r_i}^2}{r^2} \quad (2.51)$$

$$\sigma_\theta = \left(\frac{\sigma_x + \sigma_y}{2}\right)\left(1 + \frac{{r_i}^2}{r^2}\right) - \left(\frac{\sigma_x - \sigma_y}{2}\right)\left(1 + \frac{3{r_i}^4}{r^4}\right)\cos 2\theta - \tau_{xy}\left(1 + \frac{3{r_i}^4}{r^4}\right)\sin 2\theta - p_i\frac{{r_i}^2}{r^2} \quad (2.52)$$

$$\sigma_z = \sigma_{zz} - \nu\left[2(\sigma_x - \sigma_y)\frac{{r_i}^2}{r^2}\cos 2\theta + 4\tau_{xy}\frac{{r_i}^2}{r^2}\sin 2\theta\right] \quad (2.53)$$

$$\tau_{r\theta} = \left(\frac{\sigma_x - \sigma_y}{2}\right)\left(1 - \frac{3{r_i}^4}{r^4} + \frac{2{r_i}^2}{r^2}\right)\sin 2\theta + \tau_{xy}\left(1 - \frac{3{r_i}^4}{r^4} + \frac{2{r_i}^2}{r^2}\right)\cos 2\theta \quad (2.54)$$

$$\tau_{\theta z} = \left(-\tau_{xz}\sin\theta + \tau_{yz}\cos\theta\right)\left(1 + \frac{{r_i}^2}{r^2}\right) \quad (2.55)$$

$$\tau_{rz} = \left(\tau_{xz}\cos\theta + \tau_{yz}\sin\theta\right)\left(1 - \frac{{r_i}^2}{r^2}\right) \quad (2.56)$$

where σ_x, σ_y, σ_{zz}, τ_{xy}, τ_{xz}, and τ_{yz} are the in-situ stresses rotated to the borehole coordinate reference frame. Contour plots of the radial and tangential stress distributions using Equations 2.51 and 2.52 are demonstrated in Figure 2.15.

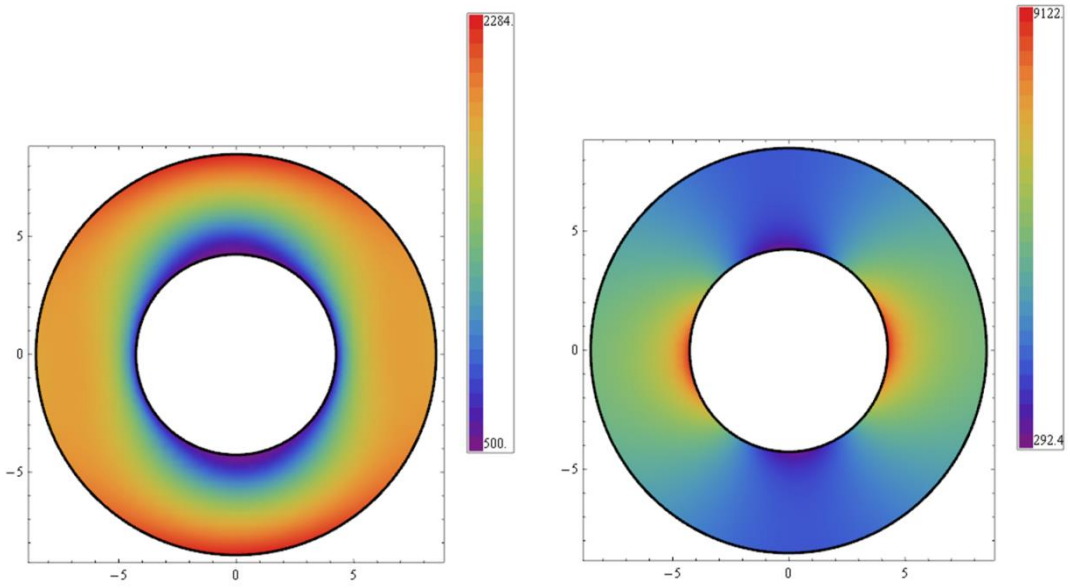

Figure 2.15: An example of radial (left) and tangential (right) stress distributions in *psi* around an inclined wellbore as described by Equations 2.51 and 2.52. This example follows the same simulation parameters presented in Table 4.2.

Chapter 3: Elasto-plastic Behavior

The material mechanical strength is a fundamental aspect of the sand production process. An accurate description of the mechanical behavior of the sand is a central component in any sand production modeling scheme. This chapter covers the mathematical formulations utilized to describe the mechanical behavior of sand in the model.

3.1 Elastic Behavior

For a linearly elastic material, the mechanical behavior can be described by Hooke's law (Rösler et al. 2010, 43-46). In its general form:

$$\sigma_{ij} = C_{ijkl}\varepsilon_{kl} \tag{3.1}$$

where Einstein summation convention applies and *i, j, k, l*=1,2,3. The tensor σ_{ij} is the Cauchy stress tensor:

$$\sigma_{ij} = \begin{pmatrix} \sigma_{11} & \sigma_{12} & \sigma_{13} \\ \sigma_{21} & \sigma_{22} & \sigma_{23} \\ \sigma_{31} & \sigma_{32} & \sigma_{33} \end{pmatrix} \tag{3.2}$$

and ε_{kl} is the strain tensor:

$$\varepsilon_{kl} = \begin{pmatrix} \varepsilon_{11} & \varepsilon_{12} & \varepsilon_{13} \\ \varepsilon_{21} & \varepsilon_{22} & \varepsilon_{23} \\ \varepsilon_{31} & \varepsilon_{32} & \varepsilon_{33} \end{pmatrix} \tag{3.3}$$

C_{ijkl} is the stiffness tensor (or the inverse of the compliance tensor), which is a tensor of the forth order with 81 components. For an isotropic material with symmetric stress and strain tensors, the relationship reduces to

$$\begin{pmatrix}\sigma_{11}\\ \sigma_{22}\\ \sigma_{33}\\ \sigma_{23}\\ \sigma_{13}\\ \sigma_{33}\end{pmatrix} = \begin{pmatrix} C_{11} & C_{12} & C_{12} & 0 & 0 & 0 \\ C_{12} & C_{11} & C_{12} & 0 & 0 & 0 \\ C_{12} & C_{12} & C_{11} & 0 & 0 & 0 \\ 0 & 0 & 0 & \frac{C_{11}-C_{12}}{2} & 0 & 0 \\ 0 & 0 & 0 & 0 & \frac{C_{11}-C_{12}}{2} & 0 \\ 0 & 0 & 0 & 0 & 0 & \frac{C_{11}-C_{12}}{2} \end{pmatrix} \begin{pmatrix}\varepsilon_{11}\\ \varepsilon_{22}\\ \varepsilon_{33}\\ \varepsilon_{23}\\ \varepsilon_{13}\\ \varepsilon_{33}\end{pmatrix} \tag{3.4}$$

The components C_{11} and C_{12} of the stiffness tensor can be expressed in terms of Young's modulus, E, and Poisson's ratio, ν:

$$C_{11} = \frac{E(1-\nu)}{(1+\nu)(1-2\nu)} \tag{3.5}$$

$$C_{12} = \frac{E\,\nu}{(1+\nu)(1-2\nu)} \tag{3.6}$$

Additionally, E and ν can expressed in terms of the bulk modulus, K, and shear modulus, G:

$$E = \frac{9\,K\,G}{3\,K+G} \tag{3.7}$$

$$\nu = \frac{3K-2G}{2(3\,K+G)} \tag{3.8}$$

Accordingly, the relationship in Equation 3.4 can also be expressed as

$$\sigma_{ij} = \left(K - \frac{2}{3}G\right)\varepsilon_{kk}\delta_{ij} + 2G\varepsilon_{ij} \tag{3.9}$$

where δ_{ij} is Kronecker delta.

3.2 POROELASTICITY

For a porous medium, the mechanical behavior is not only a function of the solid constituents, but it also depends on the void space and the fluids that saturate it. Poroelasticity refers to a branch of science that studies the mechanical behavior of an elastic porous solid saturated with a viscous fluid. This section covers

equations drawn from the theory of poroelasticity that are used in the model formulations. First, the concept of effective stress, σ_{ij}^{e}, is introduced through the equation (Fjær et al. 2008, 33):

$$\sigma_{ij}^{e} = \sigma_{ij} + \alpha\, p\, \delta_{ij} \tag{3.10}$$

in which p is the pore pressure acting in the pore space, σ_{ij} is the external stress tensor, and α is Biot coefficient (Biot, 1941). The sign convention followed in this thesis is that tensile stress and extensive strain are positive while compressive stress and strain are negative. Figure 3.1 demonstrates the positive stress components sign convention,

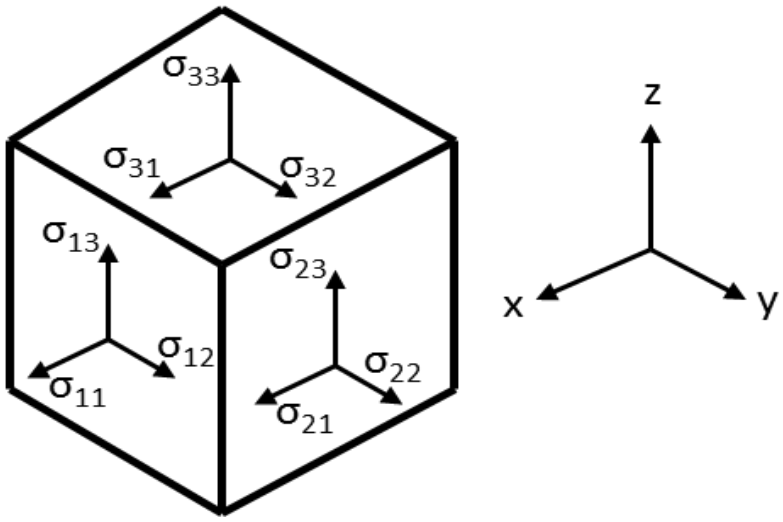

Figure 3.1: Positive stress components sign convention

The Biot coefficient is a measure of the change in pore volume relative to the change in bulk volume at a constant pore pressure. Its value is restricted in the region (Fjær et al. 2008, 33):

$$\varphi < \alpha \leq 1 \tag{3.11}$$

in which φ is the rock porosity, which is the ratio of the pore volume, V_p, to the total bulk volume, V_b:

$$\varphi = \frac{V_p}{V_b} \tag{3.12}$$

For weakly consolidated rocks the value of the Biot coefficient is close to 1. It can also be calculated according to the equation:

$$\alpha = 1 - \frac{K}{K_s} \tag{3.13}$$

In this equation (and in all future mathematical expressions presented in this thesis) K is the drained bulk modulus, also known as the frame or the skeleton bulk modulus, which refers to the bulk modulus of the evacuated porous rock. K_s refers to the bulk modulus of the solid material. The undrained bulk modulus, K_u, refers to the effective bulk modulus of a rock that is saturated with a fluid with a bulk modulus of K_f. K_u can be calculated using Gassmann's equation (Schön 2004, 251):

$$K_u = K + \frac{(1 - K/K_s)^2}{\frac{1-\varphi}{K_s} + \frac{\varphi}{K_f} - \frac{K}{{K_s}^2}} \tag{3.14}$$

Another important modulus that is used in the numerical model is the Biot modulus, M, which is defined as

$$M = \frac{K_u - K}{\alpha^2} \tag{3.15}$$

The inverse of Biot modulus corresponds to the increase in fluid volume per unit volume of rock, ζ, due to the increase of pore pressure, under a constant volumetric strain, ε, (Detournay and Cheng 1993, 118-119):

$$\frac{1}{M} = \frac{\partial \zeta}{\partial p}\Big|_{\varepsilon} \tag{3.16}$$

Using Equations 3.13 and 3.14, The Biot modulus can be expressed as

$$M = \frac{K_f}{\varphi + (\alpha - \varphi)(1 - \alpha)\left(\frac{K_f}{K}\right)} \tag{3.17}$$

3.3 Plastic Behavior

Contrary to hard rocks, unconsolidated sands experience a relatively high degree of ductility in which brittle behavior is no longer a reasonable assumption. It has been observed that mechanical failure in unconsolidated sands does not occur even if the elastic limit is surpassed (Antheunis et al. 1976). If the stress state of the material surpasses its elastic limit, which is also known as the yield strength, irreversible plastic deformation starts to develop. Consequently, the incremental strain will be composed of both elastic and plastic components (Fjær et al. 2008, 81):

$$d\varepsilon_{ij} = d\varepsilon_{ij}^{e} + d\varepsilon_{ij}^{p} \tag{3.18}$$

Therefore, it is necessary to account for plastic deformation in the sand matrix by employing a suitable plasticity model. This model has to be able to accurately predict the onset of plastic strain and its magnitude as a function of the stress state.

3.3.1 Yield Criterion

The yield point refers here to a specific state of stress in which plastic deformation starts to develop. Several yield criteria have been reported in the literature to mathematically describe the strength of granular materials such as cement, soil, and rocks. In the presented model, a Mohr-Coulomb failure criterion will be used as the basis of the mathematical formulation of the plastic model.

The reasoning behind the Mohr-Coulomb criterion originates from the mechanical behavior observed in tri-axial compression tests. In such tests, it has been observed that the rock specimens become stronger if lateral displacement is restricted by applying a confining pressure (Jaeger and Cook 1979, 86). For a linear relationship between the specimen strength and the confining pressure, the Mohr-Coulomb criterion can be expressed as

$$\tau = \sigma \tan\phi + c \tag{3.19}$$

where τ is the shear strength, σ is the normal stress across the failure plane, ϕ is the internal friction angle, c is the intercept of the failure envelope with the τ axis, commonly known as the cohesion. Furthermore, the failure criterion can be demonstrated using a Mohr circle, plotted in Figure 3.2, in which the red line represents the failure envelope.

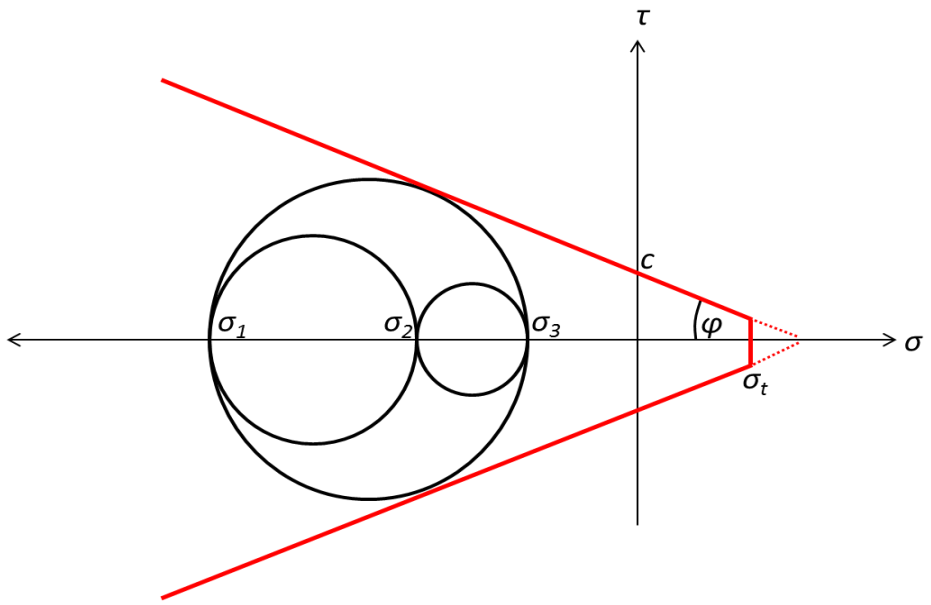

Figure 3.2: Mohr-Coulomb failure envelope

Here σ_1, σ_2, and σ_3 are the principal stresses such that

$$\sigma_3 \geq \sigma_2 \geq \sigma_1 \tag{3.20}$$

Customarily, failure criteria are expressed in the form

$$f(\sigma_{ij}) = 0 \tag{3.21}$$

If $f(\sigma_{ij}) < 0$, the material only deforms elastically, and it yields when $f(\sigma_{ij}) = 0$. Using the principal stresses to describe the stress state, σ_{ij}, Mohr-Coulomb failure criterion can be expressed as (FLAC3D User's Guide)

$$f^s = \sigma_1 - \sigma_3 N_\phi + 2c\sqrt{N_\phi} \tag{3.22}$$

N_ϕ is a function of the internal friction angle, and f^s corresponds to the shear failure criterion

$$N_\phi = \frac{1 + \sin\phi}{1 - \sin\phi} \tag{3.23}$$

Furthermore, the same failure criterion can be extended to account for tensile failure, f^t

$$f^t = \sigma_3 - \sigma^t \tag{3.24}$$

where σ^t is the tensile strength. From figure 3.2, it can be shown that the maximum tensile strength, σ^t_{max}, is the intersection of the failure envelope with the σ axis, which can be calculated from the equation below,

$$\sigma^t_{max} = \frac{c}{\tan\phi} \tag{3.25}$$

3.3.2 Plastic Flow

The amount of plastic strain developed after the material yields can be determined by employing an appropriate plastic flow rule. In plasticity theory, the flow rule describes the relationship between the stress and the plastic strain increment, $d\varepsilon^p_{ij}$, using the plastic potential function, g, (Fjær et al. 2008, 83)

$$d\varepsilon^p_{ij} = \lambda \frac{\partial g}{\partial \sigma_{ij}} \tag{3.26}$$

where λ is a proportionality factor, which is a non-negative scalar quantity that is calculated using the consistency condition.

For shear failure, the potential function, g^s, is defined as (FLAC3D User's Guide)

$$g^s = \sigma_1 - \sigma_3 N_\Psi + constant \tag{3.27}$$

N_Ψ is a constant that is dependent on the dilation angle:

$$N_\Psi = \frac{1 + \sin\Psi}{1 - \sin\Psi} \tag{3.28}$$

The dilation angle represents the ratio of plastic volume change over plastic shear strain (Vermeer and de Borst 1984). It is defined as

$$\sin\Psi = \frac{\dot{\varepsilon}^p_v}{-2\dot{\varepsilon}^p_1 + \dot{\varepsilon}^p_v} \tag{3.29}$$

where $\dot{\varepsilon}_1^p$ represents the principal plastic shear rate in the direction of the axial compressive stress and $\dot{\varepsilon}_v^p$ is the volumetric plastic strain rate calculated as,

$$\dot{\varepsilon}_v^p = \dot{\varepsilon}_1^p + \dot{\varepsilon}_2^p + \dot{\varepsilon}_3^p \tag{3.30}$$

The value for the dilation angle cannot exceed that of the friction angle, and it is considerably lower for loose sands. If $\Psi = \phi$, then the potential flow function, g, is equivalent to the yield function, f, and the rule is an associated flow rule. Otherwise, it is a non-associated flow rule. For tensile plastic strain, an associated flow rule is assumed, and the potential function is (FLAC3D User's Guide)

$$g^t = -\sigma_3 \tag{3.31}$$

3.3.3 Strain Hardening/Softening

The consistency condition states that as long as the yielding material is under loading, the stress state must stay on the failure surface and not exist outside it. In other words, only two cases can occur: $f < 0$ and $f = 0$. If the material hardens, the stress state does not leave the failure surface, but the failure surface moves according to some hardening law (Rösler et al. 2010, 85-86). Figure 3.3 illustrates this concept.

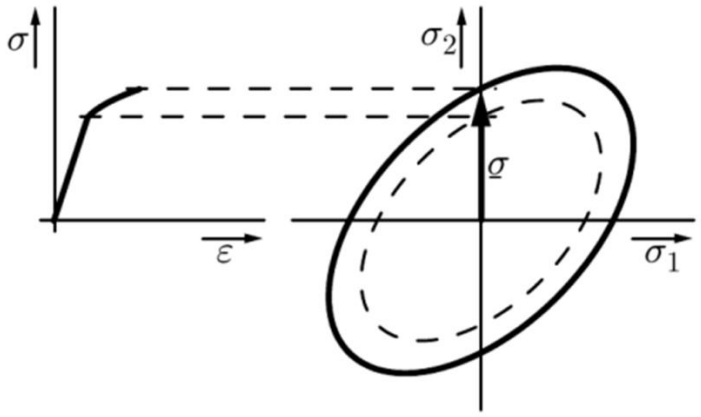

Figure 3.3: The change in yield surface during hardening (Rösler et al. 2010, 98).

Hardening laws define the change of the yield surface as a function of a hardening parameter that captures the plastic strain history. Many definitions have been used in the literature for hardening laws of granular materials.

Veermer and deBorst (1984) proposed the following definition for the hardening parameter:

$$\bar{\varepsilon}^p = \int \sqrt{\frac{2}{3}\left(\dot{\varepsilon}_1^p \dot{\varepsilon}_1^p + \dot{\varepsilon}_2^p \dot{\varepsilon}_2^p + \dot{\varepsilon}_3^p \dot{\varepsilon}_3^p\right)} dt \tag{3.32}$$

In their model, changes in the yield and potential functions are made through changes in friction angle, dilation angle, and cohesion. These constant properties are replaced by plastic strain-dependent quantities referred to as the mobilized friction angle, the mobilized dilation angle, and the mobilized cohesion, respectively. The authors suggested that the plastic regime should be modeled through friction hardening and cohesion softening. In this model, the mobilized friction angle, ϕ^*, is calculated using the formula

$$\sin\phi^* = 2\frac{\sqrt{\bar{\varepsilon}^p \varepsilon^f}}{\bar{\varepsilon}^p + \varepsilon^f}\sin\phi \tag{3.33}$$

where ε^f is a constant. The mobilized cohesion, c^*, can be calculated using the formula

$$c^* = ce^{-\left(\frac{\bar{\varepsilon}^p}{\varepsilon^c}\right)^2} \tag{3.34}$$

where ε^c is also a constant. The mobilized dilation angle can be approximated as a function of the mobilized friction angle:

$$\sin \Psi^* = \frac{\sin \phi^* - \sin \phi_{cv}}{1 - \sin \phi^* \sin \phi_{cv}} \tag{3.35}$$

where ϕ_{cv} is a constant defined as

$$\sin \phi_{cv} = \frac{\sin \phi - \sin \Psi}{1 - \sin \phi \sin \Psi} \tag{3.36}$$

Figure 3.4 shows generic plots of cohesion and friction based on Equations 3.33 and 3.34. Correspondingly, Figure 3.5 shows the results of a simulated tri-axial test using these formulations.

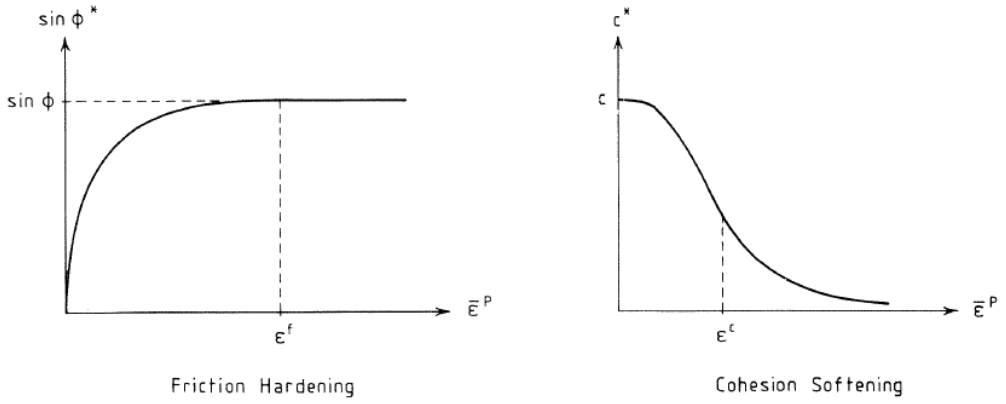

Figure 3.4: Mobilized friction and mobilized cohesion as functions of the hardening parameter (Vermeer and de Borst 1984).

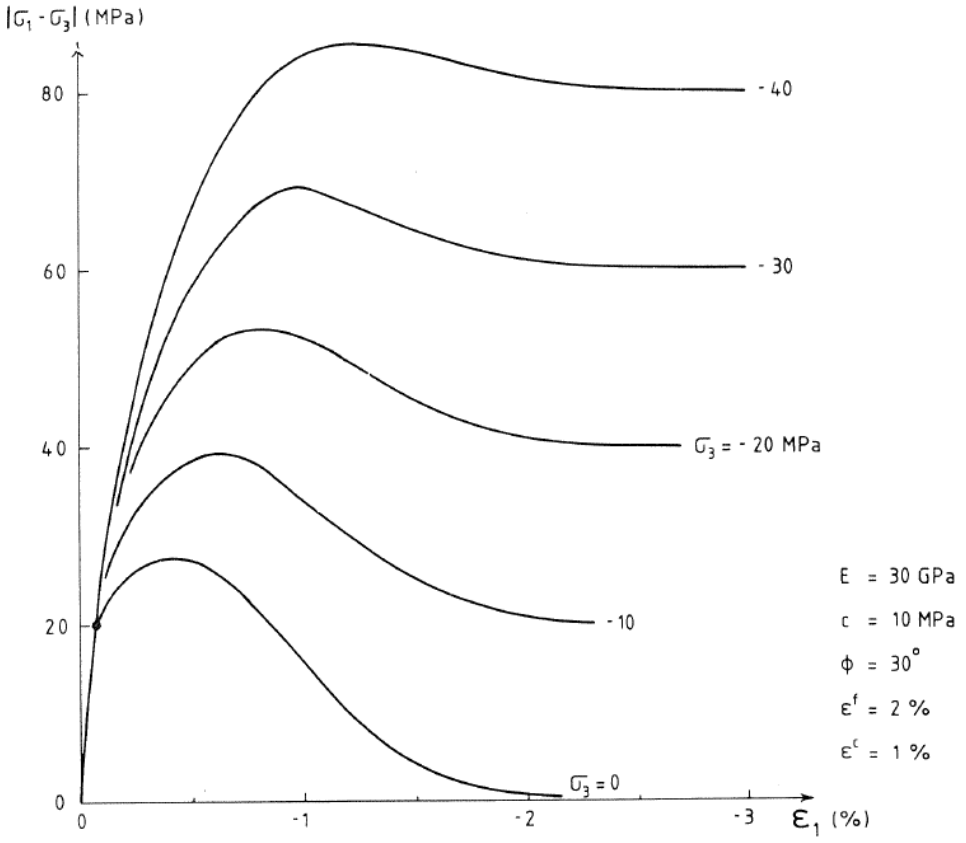

Figure 3.5: Simulated tri-axial tests based on the proposed hardening model (Vermeer and de Borst 1984).

Papanastasiou and Vardoulakis (1992) presented a Cosserat-Mohr-Coulomb elasto-plastic model in which tensile strength and the mobilized friction coefficient are functions of the plastic shear strain intensity, γ^p. This parameter can be defined by the following incremental form in the case of a symmetric plastic strain-rate tensor:

$$d\gamma^p = \sqrt{2\, de_{ij}^p\, de_{ij}^p} \tag{3.37}$$

where e_{ij}^p is the deviator plastic strain tensor, defined as

$$e_{ij}^{p} = \varepsilon_{ij}^{p} - \frac{\varepsilon_{kk}^{p}}{3}\delta_{ij} \tag{3.38}$$

Papamichos and van den Hoek (1995) calibrated the model based on triaxial tests for Berea and Castlegate sandstones assuming an associated flow rule. The following function was used to model the mobilized friction coefficient:

$$\mu = \begin{cases} \mu_0 + \dfrac{(1+\mu_3\gamma^p)\gamma^p}{\mu_1+\mu_2\gamma^p} & for\ \gamma^p \le \gamma_p^p \quad (3.39) \\ \mu_4 & for\ \gamma^p > \gamma_p^p \quad (3.40) \end{cases}$$

The mobilized friction coefficient is defined as

$$\mu = \sin\phi^* \tag{3.41}$$

Also, the following function was used to model the tensile strength

$$\sigma^t = \begin{cases} \sigma_0^t & for\ \gamma^p \le \gamma_p^p \quad (3.42) \\ \sigma_0^t - \sigma_1^t\left(\gamma^p - \gamma_p^p\right) & for\ \gamma^p > \gamma_p^p \quad (3.43) \end{cases}$$

The calibration constants presented in the Equations 3.39-3.43 in addition to the elastic properties are summarized in Table 3.1 for both Berea and Castlegate sandstone.

Table 3.1: Elasto-plastic properties for Berea and Castlegate sandstone (Papamichos and van den Hoek 1995)

Property	Value	
	Berea Sandstone	Castlegate Sandstone
Young modulus, E, GPa	17.3	6.83
Poisson's ratio, ν	0.27	0.178
σ_0^t, MPa	17.624	9.8051
σ_1^t, MPa	50.2-74.4	28.7
μ_0	0.49	0.46295
μ_1	0.0056141	0.0077
μ_2	6.6395	7.5
μ_3	-7.8494	-20.75
μ_4	0.61699	0.56263
γ_p^p	0.0069916	0.0060819

For the presented analysis, Fast Lagrangian Analysis of Continua in 3 Dimensions (FLAC3D) software package is used. In FLAC3D, strain hardening/softening formulations for Mohr-Coulomb model are described as functions of the shear strain hardening parameter, κ^s, defined in the incremental form as (FLAC3D User's Guide):

$$\Delta\kappa^s = \frac{1}{\sqrt{2}}\sqrt{(\Delta\varepsilon_1^{ps} - \Delta\varepsilon_m^{ps})^2 + (\Delta\varepsilon_m^{ps})^2 + (\Delta\varepsilon_3^{ps} - \Delta\varepsilon_m^{ps})^2} \tag{3.44}$$

in which $\Delta\varepsilon_i^{ps}$ is the principal plastic shear strain increment and $\Delta\epsilon_m^{ps}$ is the volumetric plastic shear strain increment defined as

$$\Delta\epsilon_m^{ps} = \frac{1}{3}(\Delta\varepsilon_1^{ps} + \Delta\varepsilon_3^{ps}) \tag{3.45}$$

In fact, the hardening parameter, $\Delta\kappa^s$, represents the square root of the second invariant of the deviatoric plastic shear strain increment tensor, in which $\Delta\varepsilon_2^{ps}$ is zero. The tensile hardening parameter increment is defined as

$$\Delta\kappa^s = \left|\Delta\varepsilon_3^{pt}\right| \tag{3.46}$$

Friction angle, dilation angle, cohesion, and tensile strength can all be functions of the hardening parameter and can be approximated as sets of linear segments as shown in Figure 3.6.

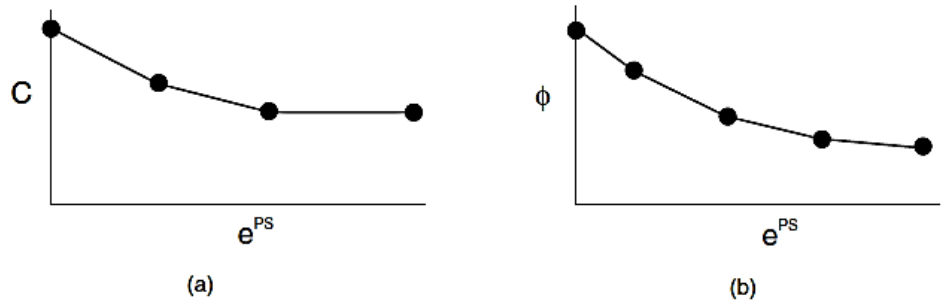

Figure 3.6: FLAC3D simulation of cohesion and friction angle as functions of the plastic strain (FLAC3D User's Guide).

3.3.4 Shear Banding

It has been observed that the mechanical failure of various types of materials is characterized by localized shear deformations (Vardoulakis and Sulem 1995, 3-4). In granular materials, failure as a result of micro-cracking and relative motion between grains may lead to intense plastic shearing and dilation inside a localized zone. The formation of shear bands is a common form in which localized failure takes place in geomaterials. These discontinuities of failed material are enclosed by elasto-plastic boundaries that propagate outward with more intensification of plastic deformation. Bifurcation analysis has been widely used by many researchers to study the occurrence and propagation of shear bands in granular materials.

Classical continuum models might be able to predict the existence of shear bands if appropriate constitutive plastic models are implemented. However, they fall short of accurately predicting the size scale of such phenomenon, and as a

consequence the thickness of the shear bands, which has been observed to be related to the grain size (Vardoulakis and Sulem 1995, 10). The reason is that classical models do not incorporate material parameters with a dimension of length. Hence, it is essential to implement continuum models that incorporate microstructural properties to accurately simulate localized failures. These models can either contain higher degrees of freedom, such as Cosserat continuum, or higher deformation gradient models.

The software used in the presented analysis, FLAC3D, is capable of predicting the development of shear bands as shown in Figure 3.7. However, similar to many classical continuum models, the shear band thickness is grid-dependent and does not account for the influence of material's microstructure.

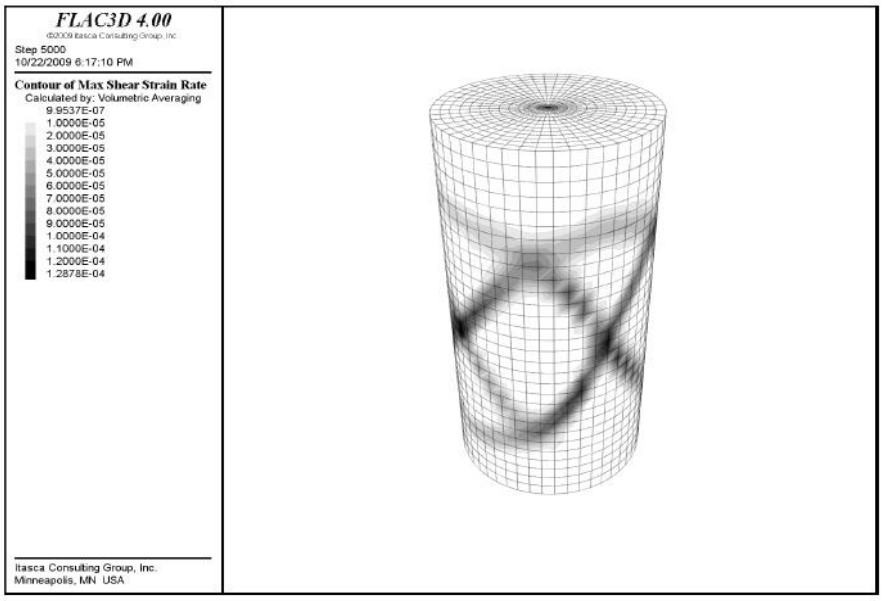

Figure 3.7: Shear band formation in a strain-softening material as simulated by FLAC3D (FLAC3D User's Guide).

Chapter 4: The In-situ Stress State

Earth in-situ stresses exist due to the weight of the overlaying rocks in addition to plate tectonic activities. The magnitude and the direction of in-situ stresses play a significant role in the sanding mechanism from oil and gas well. This chapter discusses how the earth in-situ stresses are simulated in the presented sand production model. Also, it demonstrates how three-dimensional stress transformation is performed in order to calculate the model boundary conditions for inclined wellbores and oriented perforations.

4.1 Stress Distribution in Vertical Wellbores

The coordinate system (*x, y, z*) is defined by the three principal in-situ stresses as shown in Figure 4.1. In this coordinate system, one of the principal stresses is aligned vertically (parallel to the direction of gravity), and the direction of the other horizontal stresses is known. Anisotropic horizontal stresses are considered in this model, in which the overburden stress, σ_v is parallel to the z-axis, the maximum horizontal stress, σ_H, is parallel the x-axis, and minimum horizontal stress, σ_h, is parallel to the y-axis.

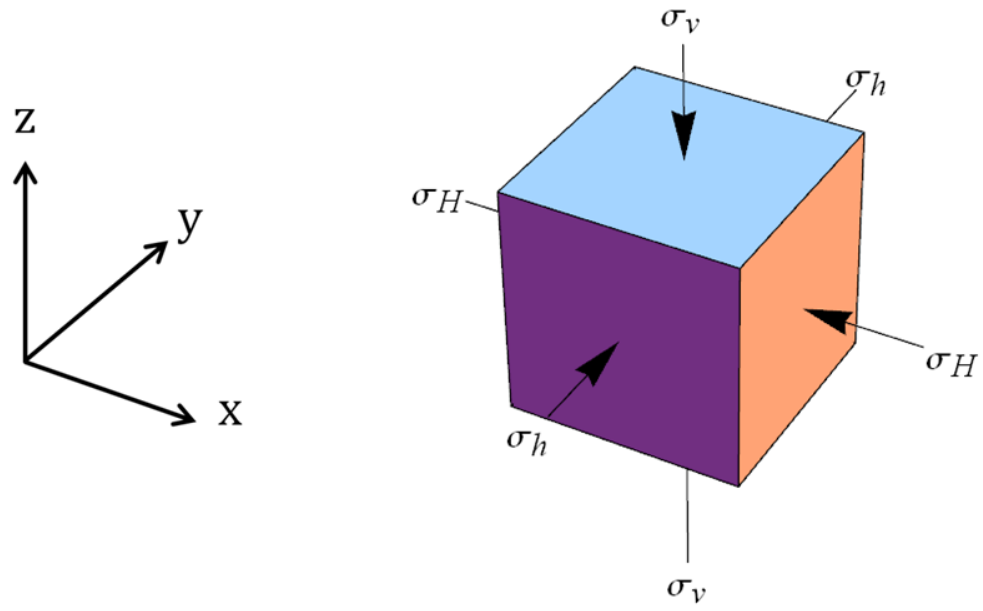

Figure 4.1: In-situ stresses in respect to the model coordinate system.

In a vertical wellbore, the stress boundary conditions of the model can be aligned with the earth in-situ principal stresses. For an elastic porous medium, stress distribution around the wellbore follows the relationship stated in Equations 2.42 and 2.43. Using FLAC3D, a numerical solution for the stress distribution around a wellbore is compared with the analytical solution. Table 4.1 shows the simulation parameters. Figure 4.3 shows the results for the radial stress, while Figure 4.4 shows the results for the tangential stress. Figures 4.5 and 4.6 show 3D contour plots of the radial and tangential stresses.

Table 4.1: Simulation parameters for stress distribution in a vertical wellbore

Parameter	Value
σ_v, psi	-5,000
σ_H, psi	-3,000
σ_h, psi	-2,000
Wellbore pressure, psi	1,500
Pore pressure, psi	1,000
Hole diameter, inches	8.5

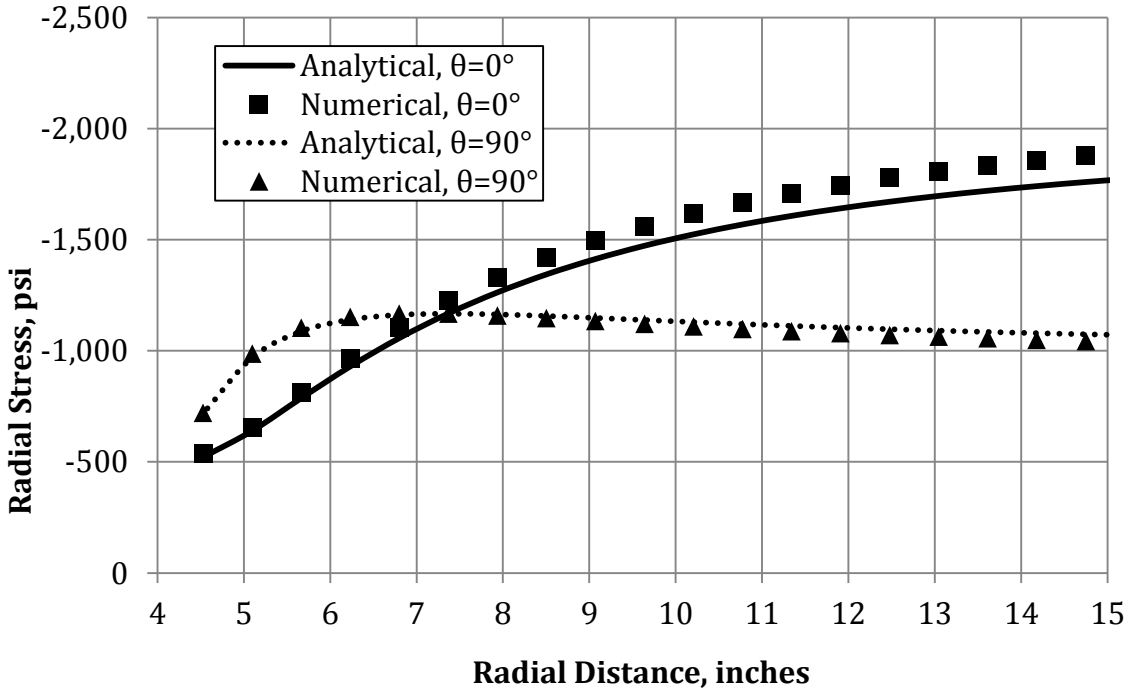

Figure 4.2: Effective radial stress versus radial distance in a vertical wellbore according to the analytical solution and FLAC3D numerical solution.

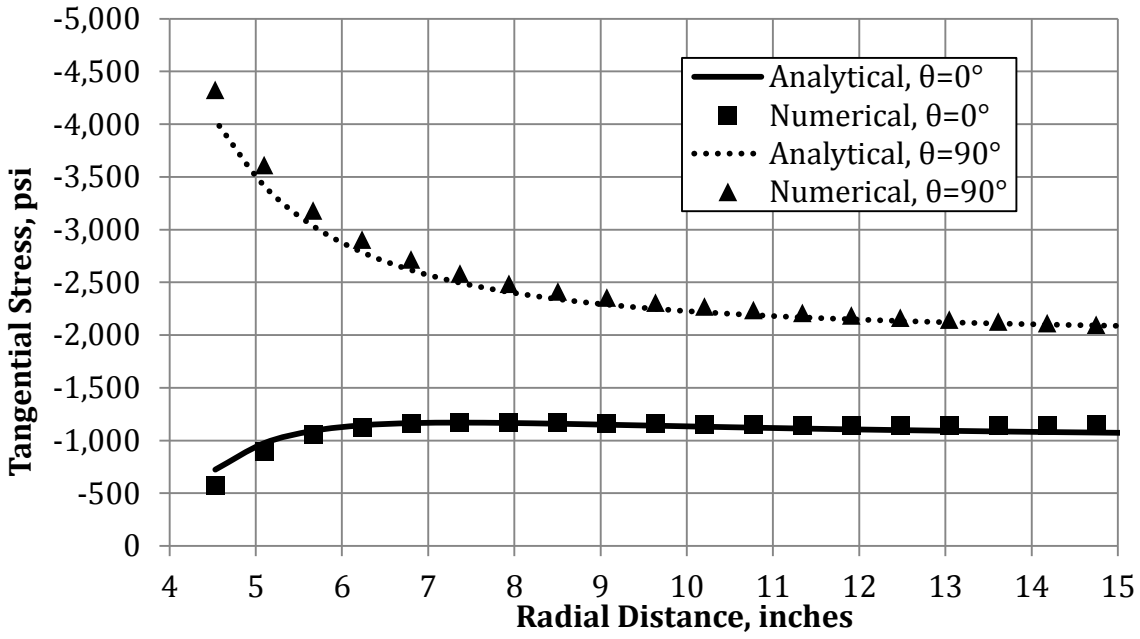

Figure 4.3: Effective tangential stress versus radial distance in a vertical wellbore according to the analytical solution and FLAC3D numerical solution.

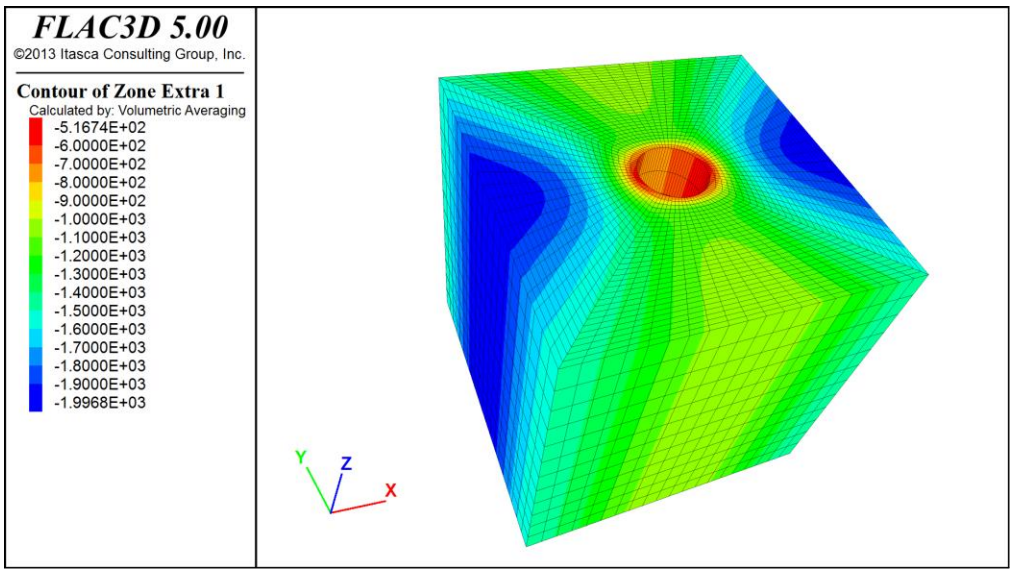

Figure 4.4: 3D contour plot of the effective radial stress distribution in a vertical wellbore.

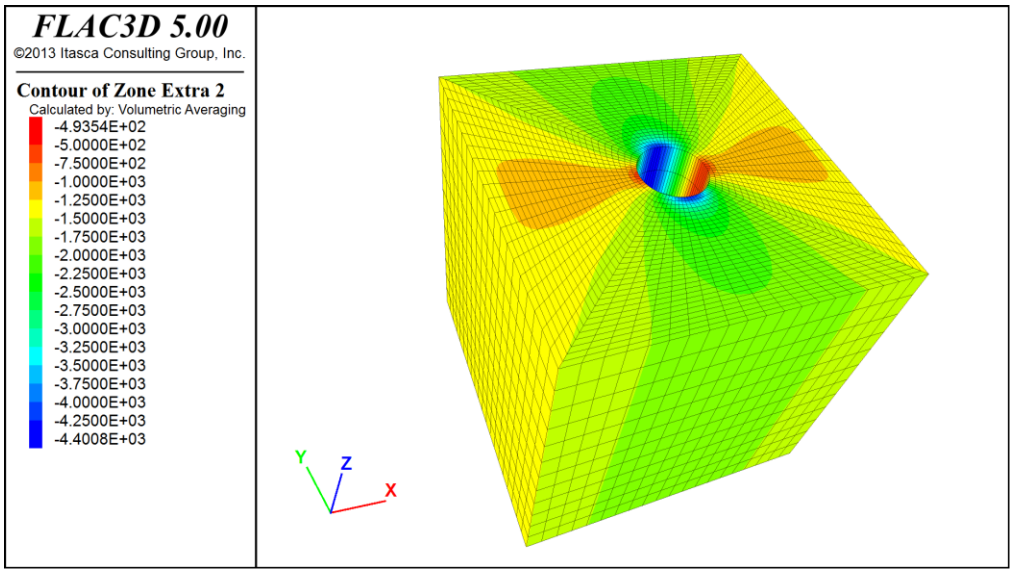

Figure 4.5: 3D contour plot of the effective tangential stress distribution in a vertical wellbore.

4.2 THREE-DIMENSIONAL STRESS TRANSFORMATION

A reference perforation tunnel that is oriented to the positive y-direction is added to the wellbore model. To transform the stresses from the coordinate system (*x,y,z*) to a new coordinate system (*x',y',z'*), the following equation is used (Rösler et al. 2010, 456).

$$\sigma'_{ij} = \boldsymbol{\alpha}.\sigma_{ij}.\boldsymbol{\alpha}^T \tag{4.1}$$

$$\begin{pmatrix} \sigma_{11} & \sigma_{12} & \sigma_{13} \\ \sigma_{21} & \sigma_{22} & \sigma_{23} \\ \sigma_{31} & \sigma_{32} & \sigma_{33} \end{pmatrix} = \boldsymbol{\alpha}.\begin{pmatrix} \sigma_H & 0 & 0 \\ 0 & \sigma_h & 0 \\ 0 & 0 & \sigma_v \end{pmatrix}.\ \boldsymbol{\alpha}^{\,T} \tag{4.2}$$

where σ'_{ij} is the stress tensor in the new coordinate system, $\boldsymbol{\alpha}$ is the orthogonal transformation matrix of which values are the direction cosines between the new and old coordinate system. All coordinate systems in this model are right-handed. The superscript T represents the transpose of the matrix. Instead of dealing with 9 angles, the elements of the transformation matrix, $\boldsymbol{\alpha}$, can be calculated using Euler angles.

While there are multiple ways to reach the desired wellbore configuration using Euler angles, *z-x-z* rotation convention will be adopted in which the following angles are defined:

β': Wellbore azimuth, measured counterclockwise from the direction of σ_H.

Ψ': The 1st rotation angle around the original z-axis. It is calculated according to the formula

$$\Psi' = \beta' - \frac{\pi}{2} \tag{4.3}$$

$\frac{\pi}{2}$ is subtracted from the wellbore azimuth in order to orient the perforation towards the original x-axis, which has the same direction as σ_H prior to rotation.

The corresponding rotation matrix is

$$\boldsymbol{\alpha_1} = \begin{pmatrix} \cos\Psi' & \sin\Psi' & 0 \\ -\sin\Psi' & \cos\Psi' & 0 \\ 0 & 0 & 1 \end{pmatrix} \tag{4.4}$$

θ': The 2nd rotation angle around the new x-axis. This angle corresponds to the wellbore inclination, measured from vertical. The corresponding rotation matrix is

$$\boldsymbol{\alpha_2} = \begin{pmatrix} 1 & 0 & 0 \\ 0 & \cos\theta' & \sin\theta' \\ 0 & -\sin\theta' & \cos\theta' \end{pmatrix} \tag{4.5}$$

φ': The 3rd rotation angle around the new z-axis. This angle corresponds to orientation of the reference perforation, measured counterclockwise from high side of the hole. In case of a vertical wellbore, this angle refers to the orientation of the reference perforation from the direction of the maximum horizontal stress in which both β' and θ' are zero. The corresponding rotation matrix is

$$\boldsymbol{\alpha_3} = \begin{pmatrix} \cos\varphi' & \sin\varphi' & 0 \\ -\sin\varphi' & \cos\varphi' & 0 \\ 0 & 0 & 1 \end{pmatrix} \tag{4.6}$$

Figure 4.6 provides a graphical representation of the angle, φ', in a deviated wellbore.

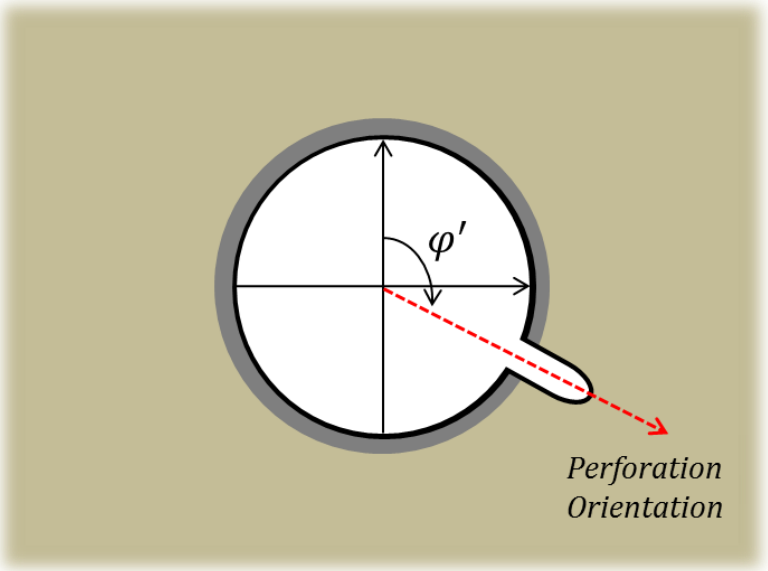

Figure 4.6: Definition of the 3rd Euler rotation angle, φ', which corresponds to the perforation orientation measured counterclockwise from the high side of the hole in a deviated well.

Based on these rotation angles, the matrix, $\boldsymbol{\alpha}$, can now be calculated

$$\boldsymbol{\alpha} = \boldsymbol{\alpha_3}.\boldsymbol{\alpha_2}.\boldsymbol{\alpha_1} \tag{4.7}$$

4.2.1 Gravitational Acceleration Vector Transformation

In a similar manner, the gravitational acceleration vector, g_i, can also be transformed using the formula

$$g_i' = \boldsymbol{\alpha}.g_i \tag{4.8}$$

in which the gravitational acceleration vector prior to rotation is expressed in the form

$$g_i = \begin{pmatrix} 0 \\ 0 \\ -9.81 \end{pmatrix}$$

4.2.2 Stress Transformation Example

Starting with in-situ principal stresses, it is possible to compute the stresses in any coordinate system as illustrated below. Let the principal earth stresses be represented by,

$$\sigma_{ij} = \begin{pmatrix} \sigma_H & 0 & 0 \\ 0 & \sigma_h & 0 \\ 0 & 0 & \sigma_v \end{pmatrix} = \begin{pmatrix} -3{,}000 & 0 & 0 \\ 0 & -2{,}000 & 0 \\ 0 & 0 & -5{,}000 \end{pmatrix}$$

The following wellbore example configuration is shown for the angles:

$$\beta' = 270° \Rightarrow \Psi' = 180°$$

$$\theta' = 60°$$

$$\varphi' = 45°$$

Graphical representation of the different rotation steps are demonstrated in Figure 4.7.

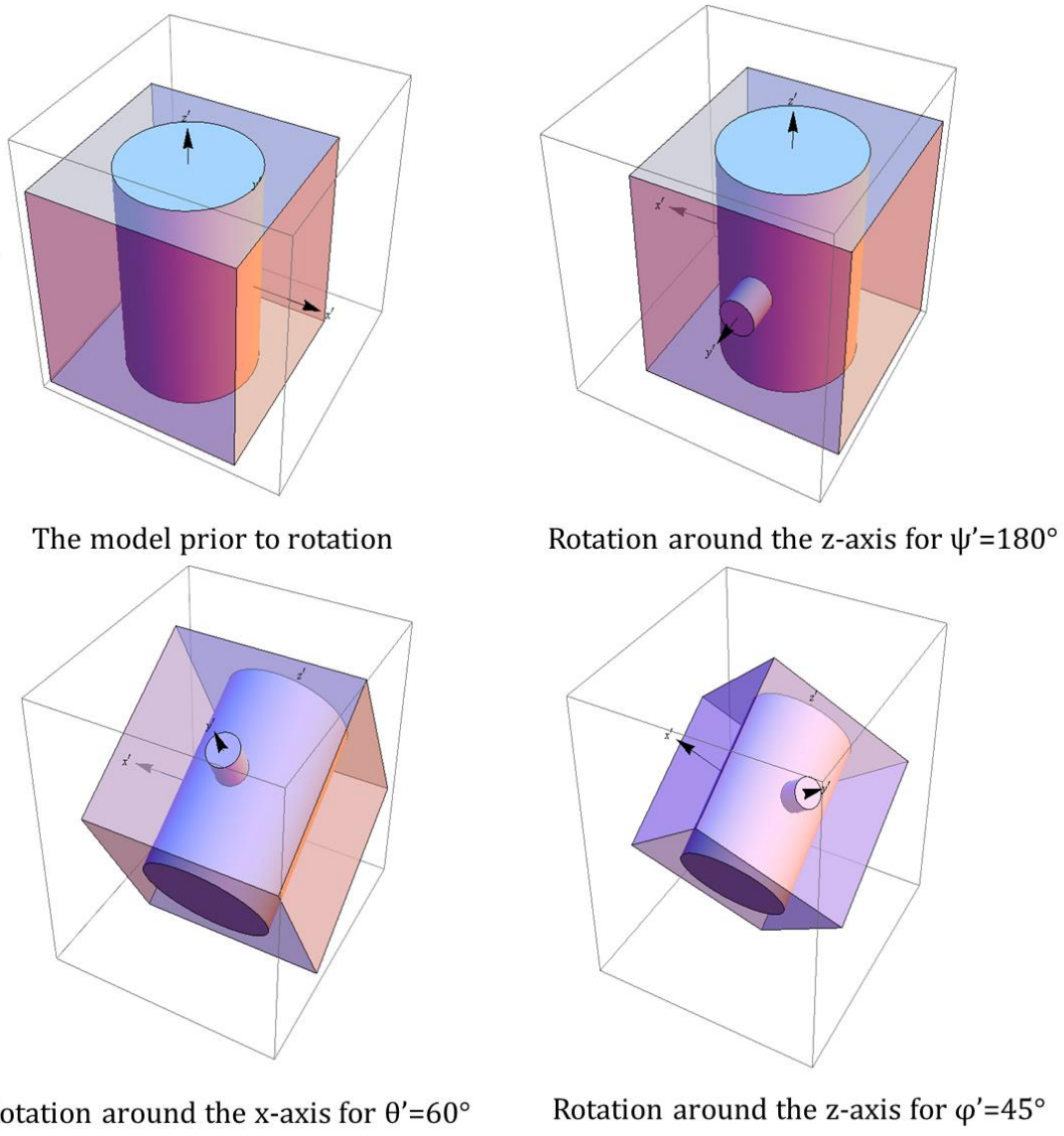

Figure 4.7: Graphical demonstration of a "z-x-z" Euler rotation of wellbore with a reference perforation.

Based on these example values and using Equations 4.1-4.7, the resulting stress boundary condition after transformations is

$$\sigma'_{ij} = \begin{pmatrix} -3{,}625 & -625 & -918.6 \\ -625 & -3{,}625 & -918.6 \\ -918.6 & -918.6 & -2{,}750 \end{pmatrix}$$

4.3 Stress Distribution in an Inclined Wellbore

For an elastic medium, the stress distribution for inclined wellbores can be computed from Equations 2.51-2.56. In this section the analytical solution is compared the numerical solution for the stress distribution obtained from FLAC3D. Stress transformation was performed in the same manner demonstrated in the previous example. Table 4.2 shows the simulation parameters. Figure 4.8 shows the results for the radial stress, while Figure 4.9 shows the results for the tangential stress. Figures 4.10 and 4.11 show 3D contour plots of the radial and tangential stresses.

Table 4.2: Simulation parameters for stress distribution in an inclined wellbore

Parameter	Value
σ_v, psi	-5,000
σ_H, psi	-3,000
σ_h, psi	-2,000
β, degrees	45°
θ, degrees	70°
Wellbore pressure, psi	1,500
Pore pressure, psi	1,000
Hole diameter, inches	8.5

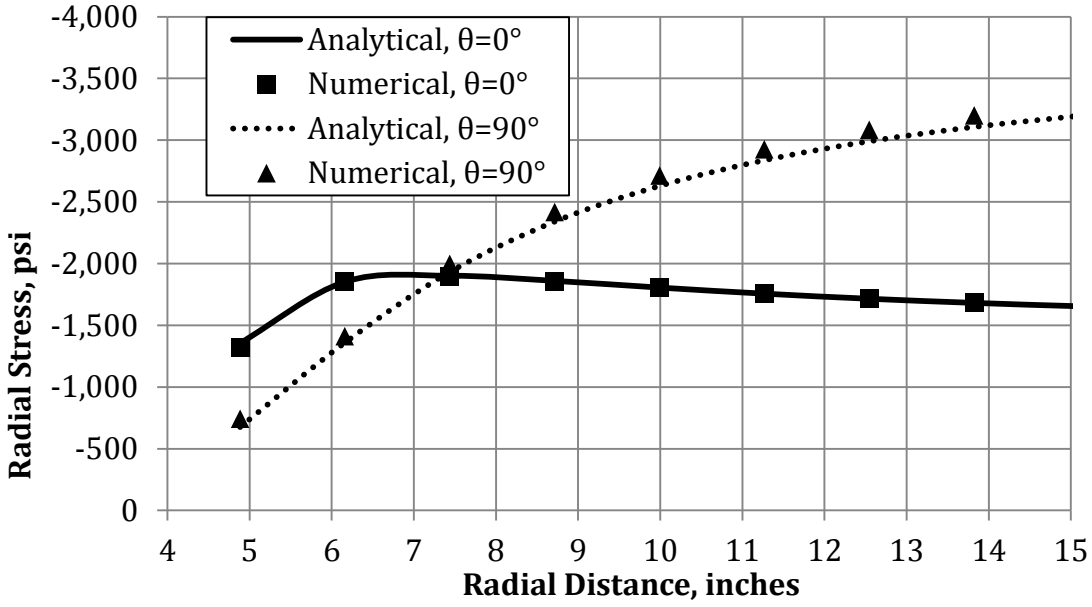

Figure 4.8: Effective radial stress versus radial distance in an inclined wellbore according to the analytical solution and FLAC3D numerical solution.

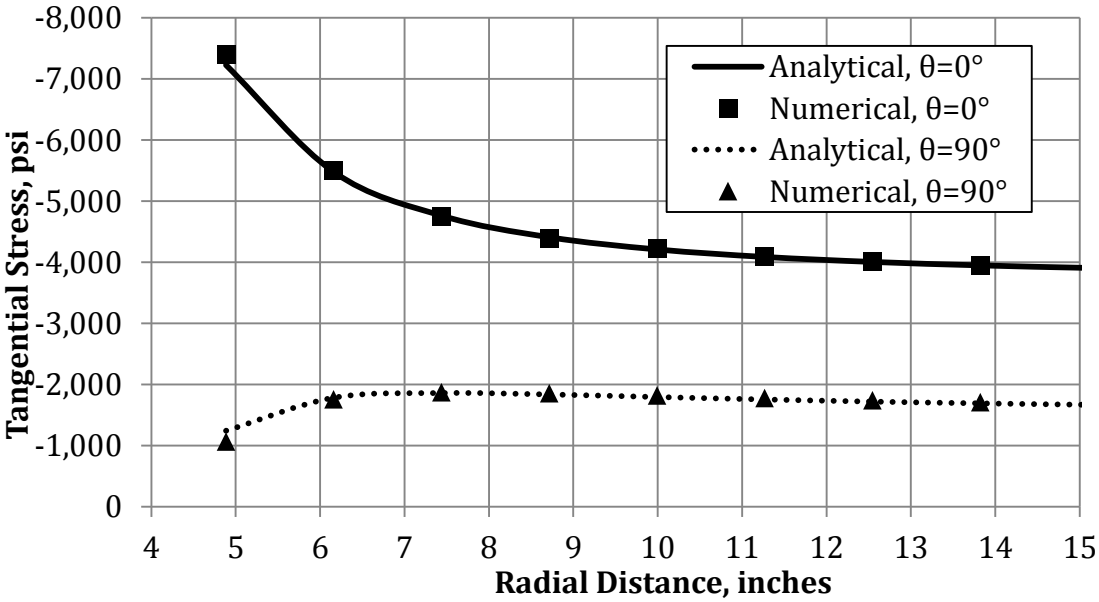

Figure 4.9: Effective tangential stress versus radial distance in an inclined wellbore according to the analytical solution and FLAC3D numerical solution.

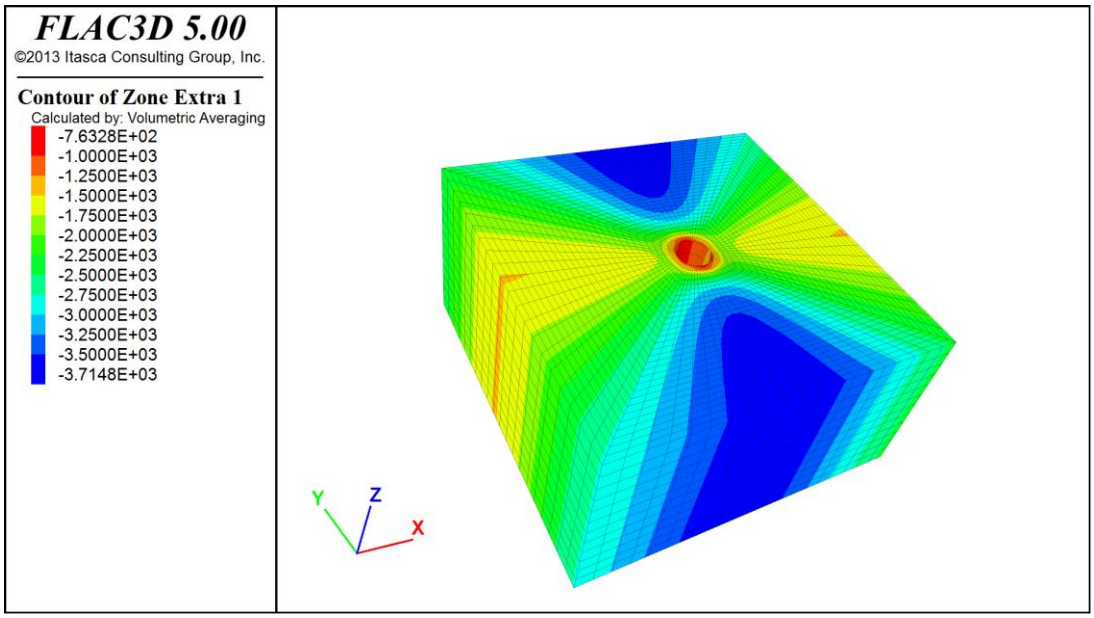

Figure 4.10: 3D contour plot of the effective radial stress distribution in an inclined wellbore.

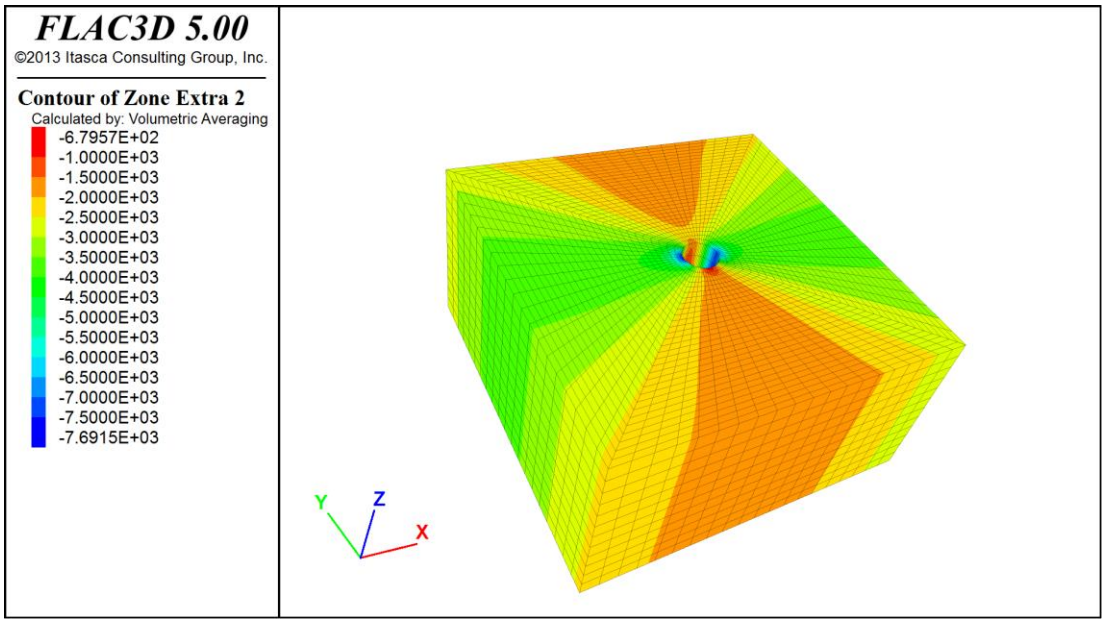

Figure 4.11: 3D contour plot of the effective tangential stress distribution in an inclined wellbore.

Chapter 5: Model Description

This chapter describes the major computational components of the model. The first two sections cover the mechanical and fluid formulations performed using FLAC3D. The third section describes the logic followed in calculating the sand erosion rate. The last section describes the different geometrical mesh models that were built for the purpose of this research. Application of boundary conditions, material constants, the simulation structure, and the erosion criterion were coded using FLAC3D programming language, *FISH*.

5.1 Mechanical Formulation

FLAC3D employs an explicit finite difference method as the basis of its calculations. Readers are advised to refer to FLAC3D User's Guide for more details concerning the explicit finite difference method. The major physical principles followed in FLAC3D calculations are shown in this section. First, the strain rate tensor, ξ_{ij}, is defined as

$$\xi_{ij} = \frac{1}{2}\left(\frac{\partial v_i}{\partial x_j} + \frac{\partial v_j}{\partial x_i}\right) \tag{5.1}$$

where v_i is the velocity vector, and x_i is the displacement vector. The rate of rotation tensor, ω_{ij}, is defined as

$$\omega_{ij} = \frac{1}{2}\left(\frac{\partial v_i}{\partial x_j} - \frac{\partial v_j}{\partial x_i}\right) \tag{5.2}$$

Cauchy's equation of motion, based on momentum balance, is

$$\frac{\partial \sigma_{ij}}{\partial x_j} + \rho b_i = \rho \frac{dv_i}{dt} \tag{5.3}$$

where b_i corresponds to the body force per unit mass, ρ is the density, and is t time.

Based on the material condition, whether it is still in the elastic regime or experiencing plastic flow, the co-rotational stress tensor is calculated from the function, H_{ij}

$$[\check{\sigma}] = H_{ij}(\sigma_{ij}, \xi_{ij}, \kappa) \tag{5.4}$$

κ is a parameter that captures the loading history. The formulations for the constitutive relations relating stress and strain were discussed in chapter 3. The components of co-rotational stress tensor are defined as

$$[\check{\sigma}] = \frac{d\sigma_{ij}}{dt} - \omega_{ik}\sigma_{kj} + \sigma_{ik}\omega_{kj} \tag{5.5}$$

These formulations contain 15 unknowns: 6 components of the stress tensor, 6 components of the strain rate tensor, and 3 components of the velocity vector. The Equations 5.1, 5.3, and 5.4 provide the 15 equations needed to solve the system. All calculations involving stress, deal with the effective stress described in Equation 3.10.

5.2 Fluid Flow Formulations

Fluid transport is mathematically modeled in accordance with Darcy's law. For a fully saturated medium with a fluid of density of ρ_f and a viscosity of μ, the specific discharge vector, q_i, can be defined as

$$q_i = -\frac{k_{il}}{\mu}\frac{\partial}{\partial x_l}\left(p - \rho_f x_j g_j\right) \tag{5.6}$$

where k_{il} is the permeability tensor, p is the pore pressure, and g_j is the gravitational acceleration vector. The mass balance for the fluid phase can be expressed as

$$-\frac{\partial q_i}{\partial x_i} + q_v = \frac{\partial \zeta}{\partial t} \tag{5.7}$$

where ζ is the variation of fluid content and q_v is the volumetric fluid source intensity. For a fully saturated medium, the change in pore pressure can be calculated using the equation

$$\frac{1}{M}\frac{\partial p}{\partial t} = \frac{\partial \zeta}{\partial t} - \alpha \frac{\partial \epsilon}{\partial t} \tag{5.8}$$

where ϵ is the volumetric strain and M is Biot modulus describes by Equation 3.16. The co-rotational stress tensor shown in Equation 5.4 is now re-expressed in the form

$$[\breve{\sigma}] + \alpha \frac{\partial p}{\partial t}\delta_{ij} = H_{ij}(\sigma_{ij}, \xi_{ij}, \kappa) \tag{5.9}$$

5.2.1 Time Scale and Coupled Simulation

Coupling between the mechanical and flow calculations is needed due to the mechanical interaction between the fluid and solid phases. This interaction presents itself in two ways. First, the effective stress is calculated based on the fluid pore pressure and Biot coefficient as shown in Equation 3.10. Second, changes in solid volume (volumetric stain) causes a change in pore pressure. Fully coupled simulation between the two different processes is especially critical when the time scale for both processes is relatively comparable. For the mechanical process, the characteristic time scale is

$$t_c^m = \sqrt{\frac{\rho}{K_u + 4/3G}}\, L_c \tag{5.10}$$

For the fluid diffusion process, the characteristic time is

$$t_c^f = \frac{{L_c}^2}{c} \tag{5.11}$$

in which c is the diffusivity. For a coupled analysis, it is defined as

$$c = \frac{k}{\frac{1}{M} + \frac{\alpha^2}{K + 4G/3}} \tag{5.12}$$

In case of a large contrast in the time scale between the two processes, fluid flow calculations can be done separately to generate pore pressure, and mechanical calculations is performed subsequently. For fluid flow only calculations, an implicit scheme could also be used for more computational efficiency.

5.3 SAND EROSION

The present work extends the use of the model developed by Kim (2010). In the model developed here, a radially-meshed evaluation zone is created around the wellbore or the perforation tunnel in which the erosion criterion specified in Equation 2.29 is invoked after each perturbation to the system. For a grid-block to be examined by the erosion criterion, it needs to be both exposed to the cavity and mechanically failed (experienced some degree of plastic strain development). For example, if the flowing bottom-hole pressure is lowered by a certain value, fluid and mechanical calculations are performed until equilibrium is reached and grid-blocks experiencing plastic flow are identified. The erosion criterion is then evoked in which the zones that meet the criterion are eroded (deleted) from the model. If some zones are eroded, the newly-exposed zones are inspected for erosion as well. This process is repeated until no more sand can be produced and the structure is both mechanically and hydraulically stable.

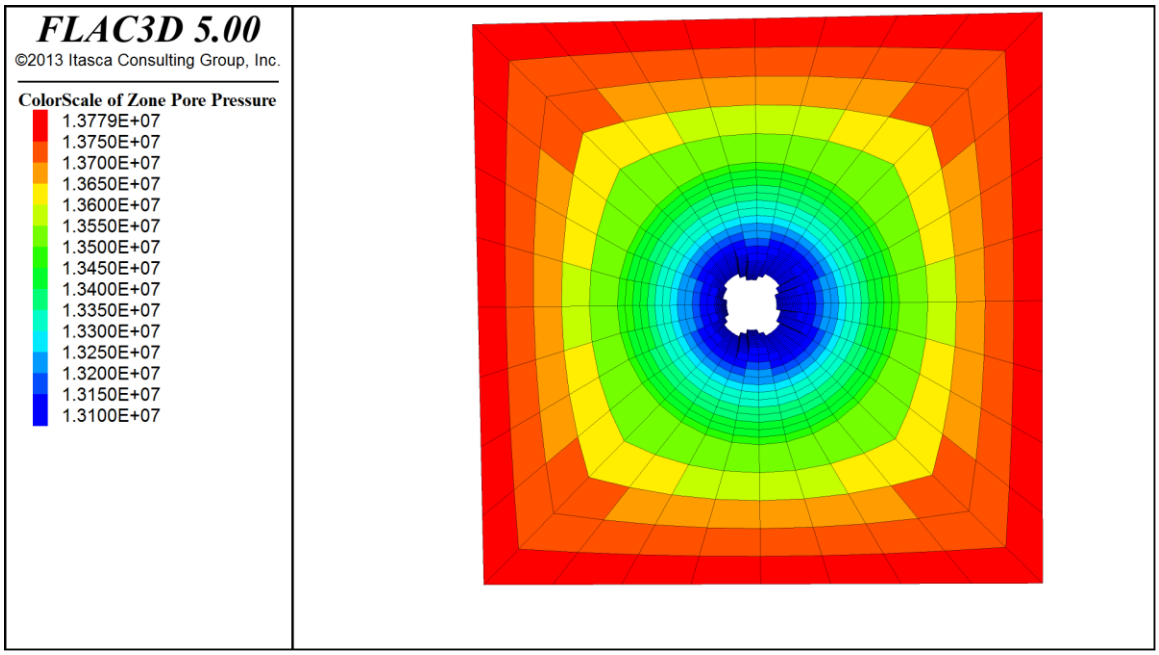

Figure 5.1: An example of sand being eroded around a wellbore as simulated by the model. The color scale shows the pore pressure distribution.

5.4 GEOMETRICAL MODELS

Three general models were designed for the purpose of this research: a wellbore model to simulate sanding from open-holes, a perforation model to simulate sanding from a single perforation tunnel, and a multi-perforation model to study the effect of perforation spacing on the mechanical stability of perforations. Below is a description of each model.

5.4.1 Wellbore Model

This geometrical model represents a cylindrical tunnel centered in a radially-gridded rectangular hexahedron. An evaluation zone is created around the wellbore cavity to evaluate its sanding profile. Stress boundary conditions are applied based on the wellbore inclination and azimuth, in-situ stresses, and wellbore pressure.

Pressure boundary conditions are applied based on the reservoir pressure and the drawdown. Figure 5.2 demonstrates a simple wellbore model in which the green portion represents the sanding evaluation zone.

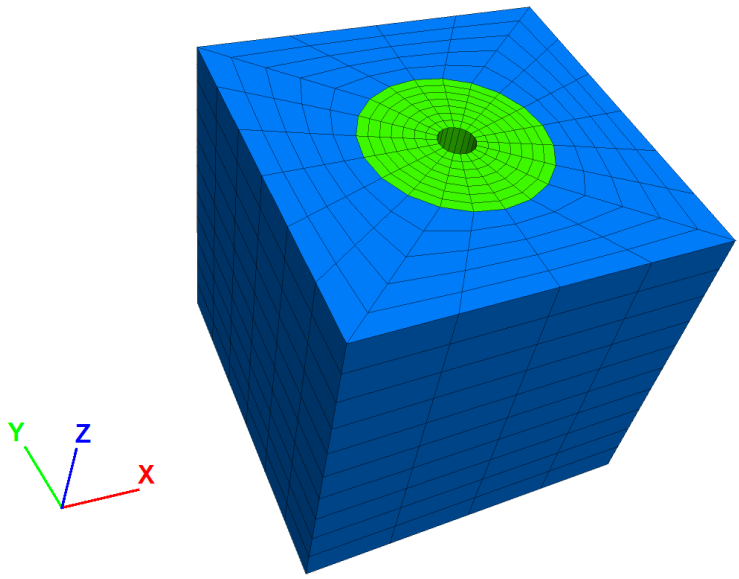

Figure 5.2: Wellbore geometrical model.

5.4.2 Single Perforation Model

As shown in section 2.3, the existence of a wellbore causes a distortion of stresses in its vicinity. Therefore, accurate description of stress distribution in the mesh necessitates the inclusion of the wellbore to study the mechanical stability in the perforation tunnel. This model is composed of two circular tunnels intersecting orthogonally; the two tunnels represent the wellbore and perforation cavities. A radially meshed evaluation zone is created around the perforation tunnel to

evaluate its sand production. The wellbore, the perforation, and the evaluation zone are enclosed in a larger structure composed of tetrahedral grid-blocks. A no-displacement boundary condition is imposed on the wellbore walls to simulate the well casing. Figure 5.3 represents a graphical representation of the model. The top-left display shows the wellbore and the perforation, where the enclosing structure and the evaluation zone are made transparent. The top right display shows the evaluation zone around the perforation tunnel, and the bottom display shows the model exterior.

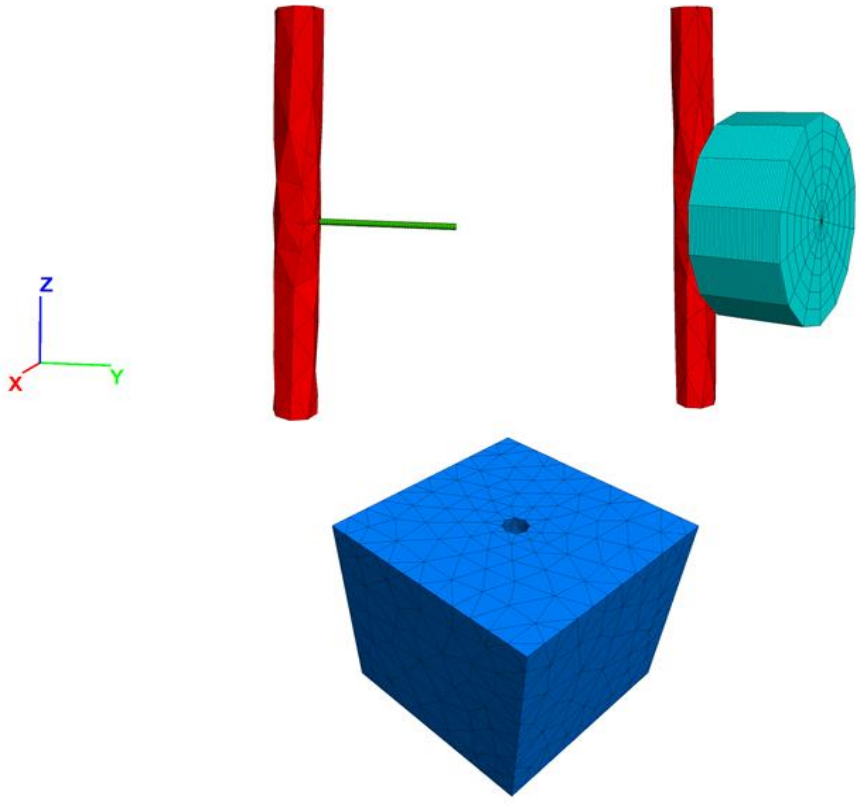

Figure 5.3: Single perforation geometrical model.

5.4.2.1 Model Meshing

Advanced meshing techniques were needed for the single perforation and the multiple-perforation models. The relatively simple meshing schemes in FLAC3D do not have the required capability to create such complex structures. Therefore, ANSYS, which is finite element software, was utilized to construct the model geometries and grid-structures. A code using *Visual Basic* was developed to convert the ANSYS meshes into FLAC3D meshes. Utilizing this technique, efficient models with considerable numerical stability and reasonable computational time were generated. The model does not contain any hanging nodes; all internal grid-points are shared between the neighboring blocks' vertices. This type of mesh minimizes stress and displacement discontinuities. The generated ANSYS models need to contain the same basic primitive mesh shapes that FLAC3D accepts: bricks, pyramids, tetrahedrons, wedges, and degenerate bricks; however, only the first three shapes were actually utilized in the models presented in this thesis. Nodal mixed discretization (NMD) computational scheme was implemented for the tetrahedral elements (Detournay and Dzik 2006).

The two software programs number the vertices of each shape differently. The created code reassigns the grid-points to the shapes' vertices according to FLAC3D format. Figure 5.4 provides an example of the difference in numbering vertices between ANSYS and FLAC3D for a hexahedral shape.

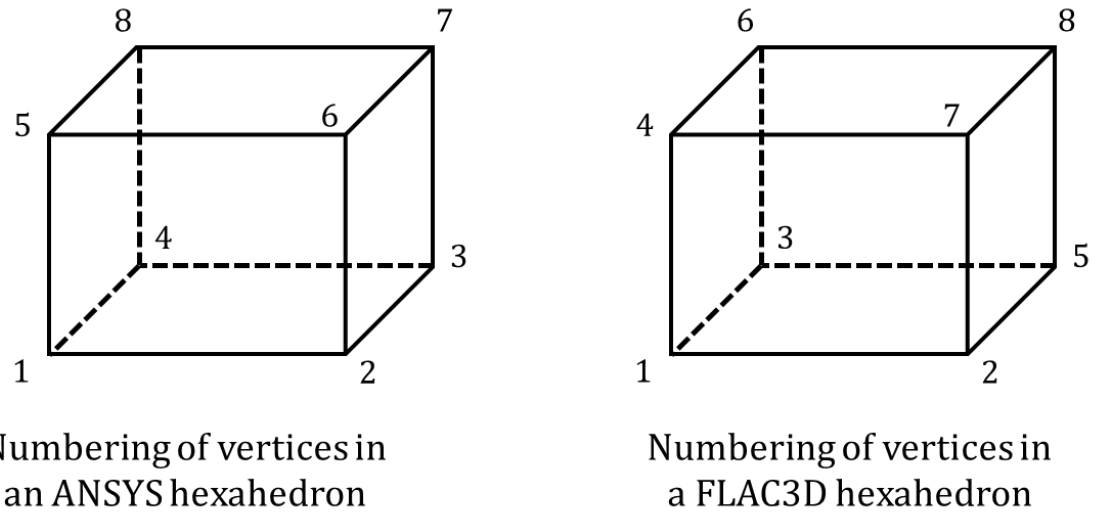

Figure 5.4: Difference in numbering vertices between ANSYS and FLAC3D for a hexahedral shape.

5.4.3 Multiple Perforation Model

A wellbore with multiple perforations is modeled to simulate mechanical instabilities around the perforation tunnel due to mechanical and hydraulic interaction from the neighboring perforations. In this model, sanding rate is not evaluated; however, the development of plastic strain in the zones surrounding each perforation is tracked. Higher plastic flow generated around the perforation walls is a sign of higher mechanical instability leading to higher probability of collapse. Figure 5.5 shows a multiple perforation model with 6 shots-per-foot (SPF) at 60° phasing.

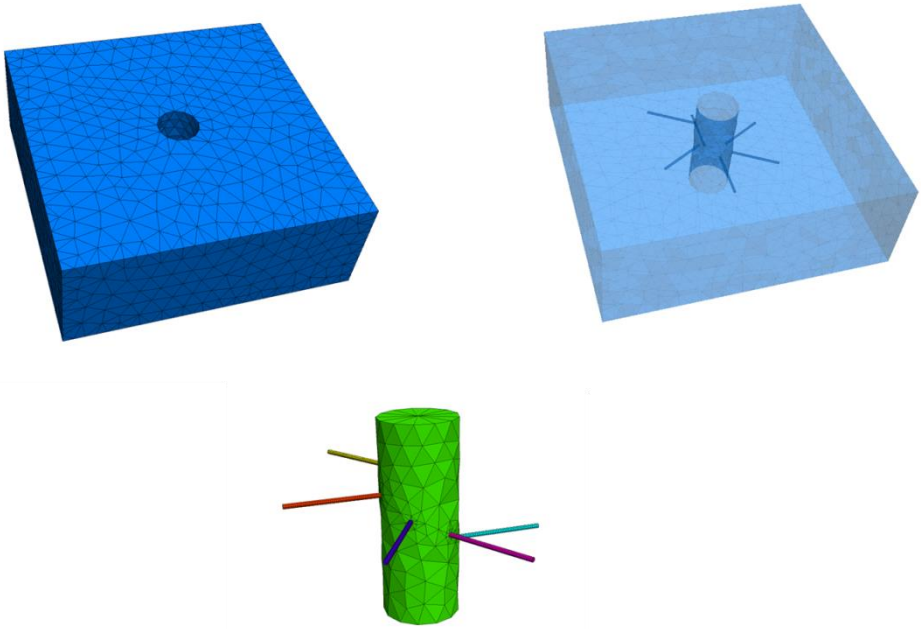

Figure 5.5: Multiple perforation geometrical model.

Chapter 6: Results and Conclusions

6.1 Simulation Results

The model was used to simulate different scenarios in order to study the effect of the wellbore configuration on sand production and perforation stability. Graphical representations for the different runs are demonstrated in the following sections. Mechanical behavior of the Castlegate sandstone as shown in Table 3.1 is assumed as a base case. Table 6.1 below shows the fluid flow properties.

Table 6.1: Fluid flow properties used in the simulation runs

Parameter	Value
Permeability, k, millidarcy	646
Viscosity, μ, cp	1.0
Porosity, φ	0.26
Fluid bulk modulus, K_f, GPa	1.0

6.1.1 Wellbore Model

The wellbore model was run at various inclination and azimuth values. Table 6.2 shows the simulation parameters while Figure 6.1 shows cumulative sand production versus wellbore drawdown pressure.

Table 6.2: Simulation parameters used for the wellbore model

Parameter	Value
σ_v, psi	-5,500
σ_H, psi	-4,000
σ_h, psi	-2,500
Pore pressure, psi	1,500
Wellbore diameter, inches	8.5
Wellbore length, ft	30

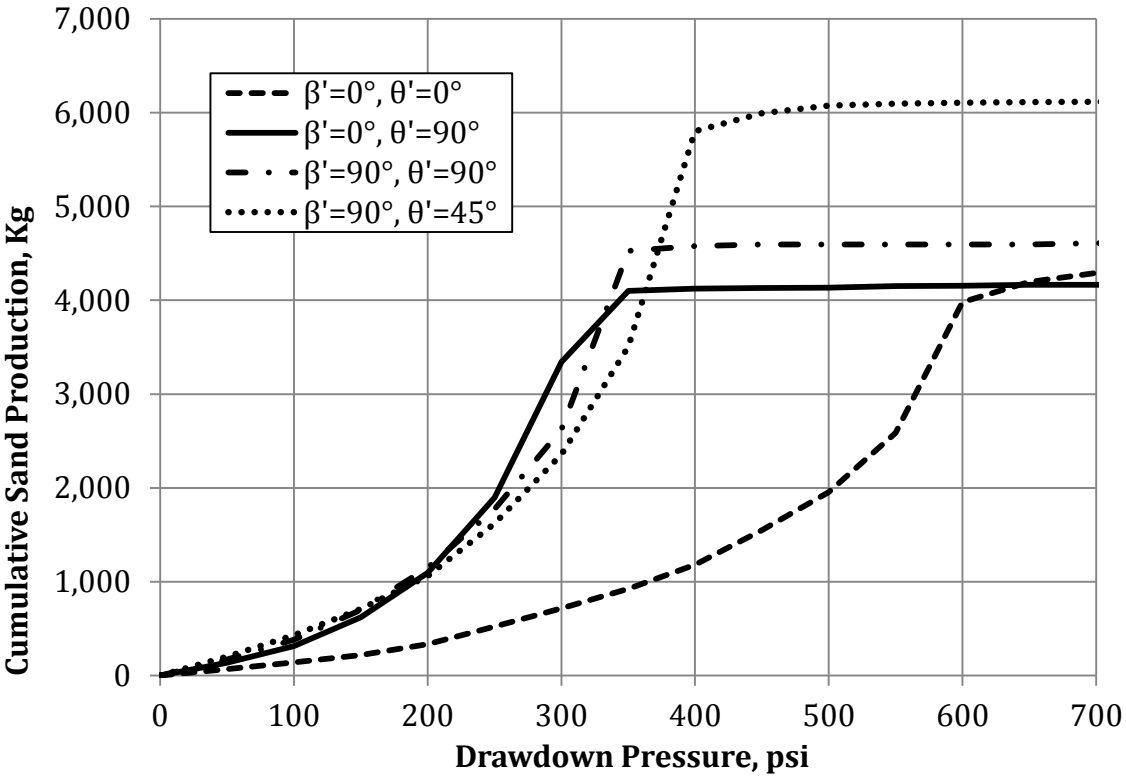

Figure 6.1: Cumulative sand production predicted by the model as a function of drawdown pressure at different wellbore orientations.

The effect of reservoir pressure depletion was also studies for the same cases simulated in Figure 6.1. Drawdown pressure was kept constant at 200 psi and the reservoir pressure was depleted from the original reservoir pressure of 1,500 psi. The simulation results are shown in Figure 6. 2.

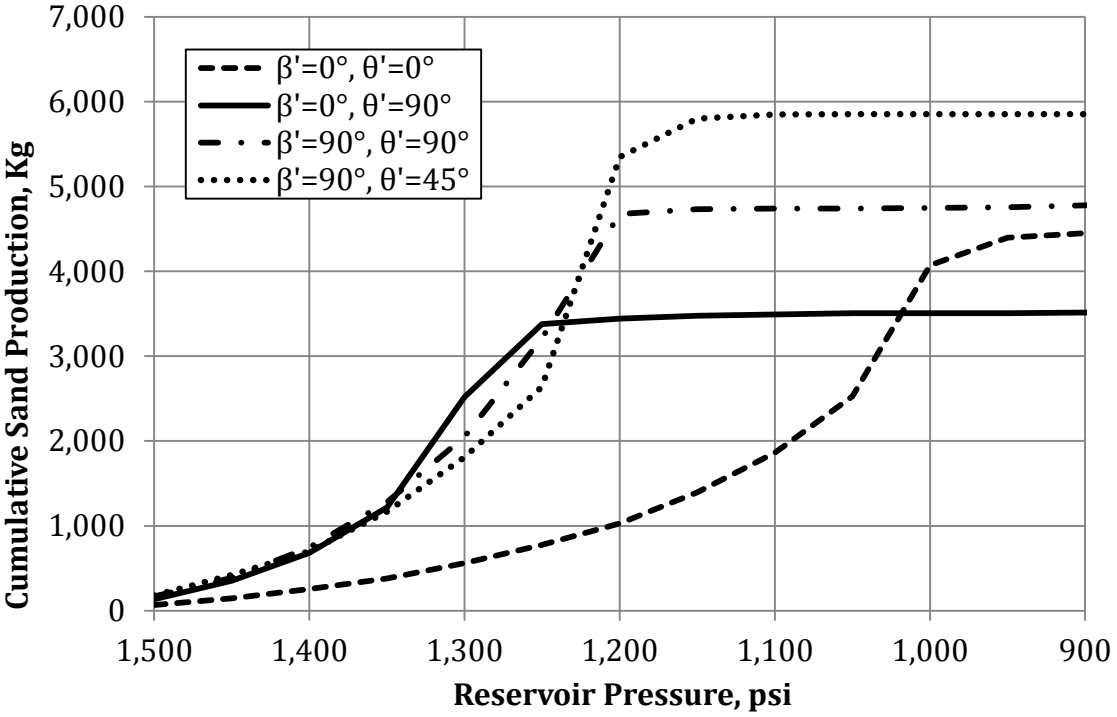

Figure 6.2: Cumulative sand production predicted by the model as a function of reservoir pressure at different wellbore orientations.

6.1.2 Single Perforation Model

In this section, sanding from a single perforation is computed as a function of drawdown pressure for different wellbore configurations. The simulation results for a horizontal wellbore are shown in Figure 6.3, and for a vertical wellbore in Figure 6.4.

Table 6.3: Simulation parameters used for the single perforation model

Parameter	Value
σ_v, psi	-6,000
σ_H, psi	-4,000
σ_h, psi	-3,000
Pore pressure, psi	1,500
Wellbore diameter, inches	8.5
Perforation diameter, inches	1.0
Perforation length, inches	23

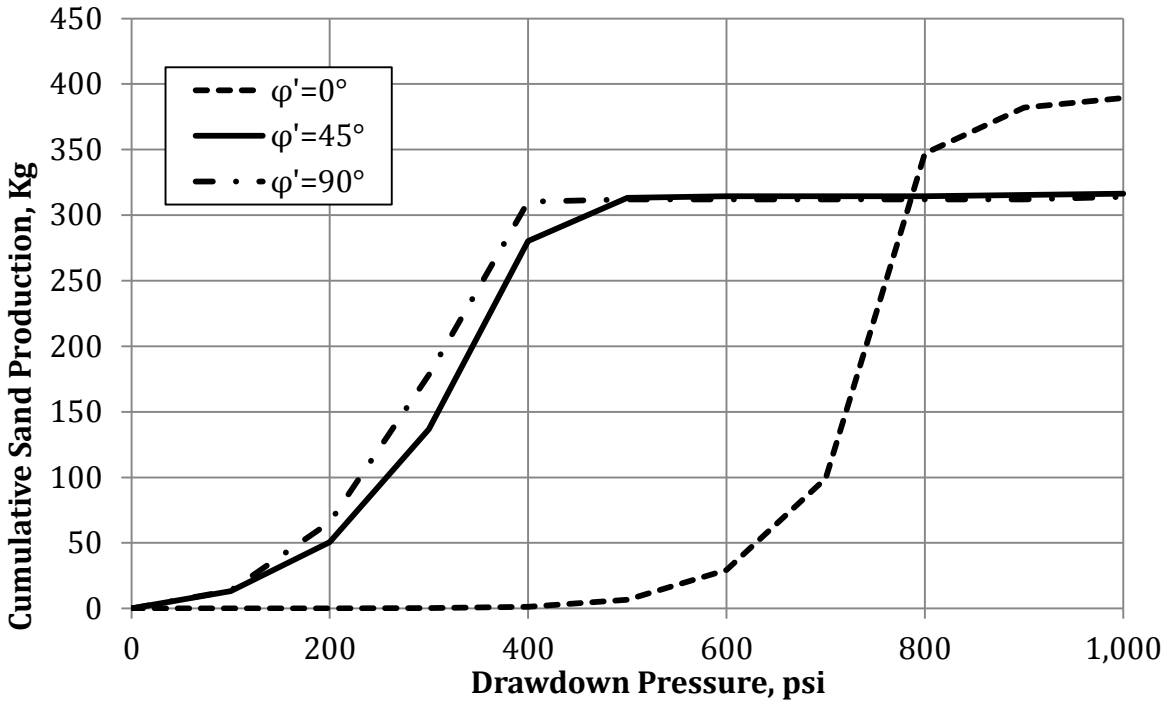

Figure 6.3: Cumulative sand production as a function of drawdown pressure at different perforation orientations for a horizontal wellbore drilled in the direction of the minimum horizontal in-situ stress ($\beta = 90°, \theta = 90°$).

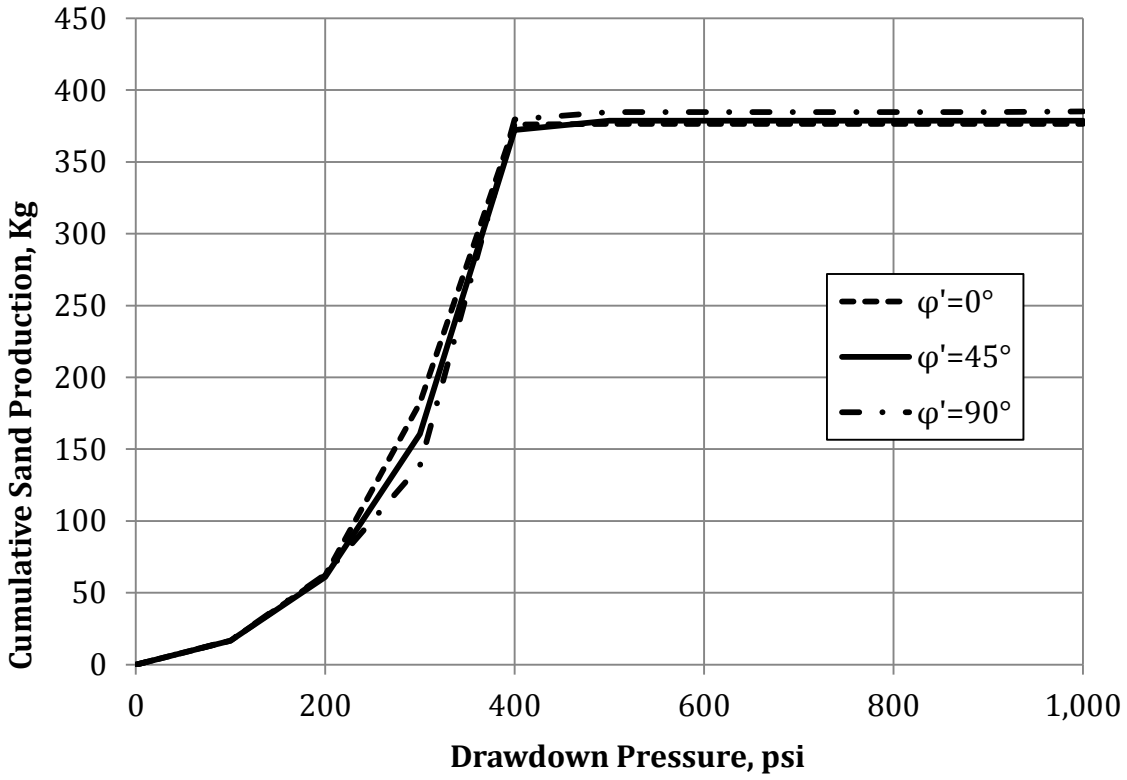

Figure 6.4: Cumulative sand production as a function of drawdown pressure at different perforation orientations for a vertical wellbore ($\beta = 0°, \theta = 0°$).

6.1.3 Multiple Perforation Model

The well is kept vertical with isotropic in-situ horizontal stresses in all the runs in order to solely investigate the hydraulic and mechanical interference from neighboring perforations. The evolution of plastic strain is studied as a function of drawdown for different wellbore configurations. In the different runs, the plastic shear strain was averaged for the grid-blocks along the cavity of the middle perforation and plotted as a function of drawdown.

Table 6.4: Simulation parameters used for the multiple perforation model

Parameter	Value
σ_v, psi	-8,000
σ_H, psi	-3,000
σ_h, psi	-3,000
Pore pressure, psi	2,000
Perforation diameter, inches	1.0
Perforation tunnel length, inches	10.0
Wellbore diameter (base case), inches	8.5
Perforation phasing (base case), degrees	90°
Perforation density (base case), shots-per-foot (SPF)	6

6.1.3.1 Effect of Phasing

Three cases with perforation phasing angle of 60°, 90°, and 180° were simulated. The results are shown in Figure 6.5.

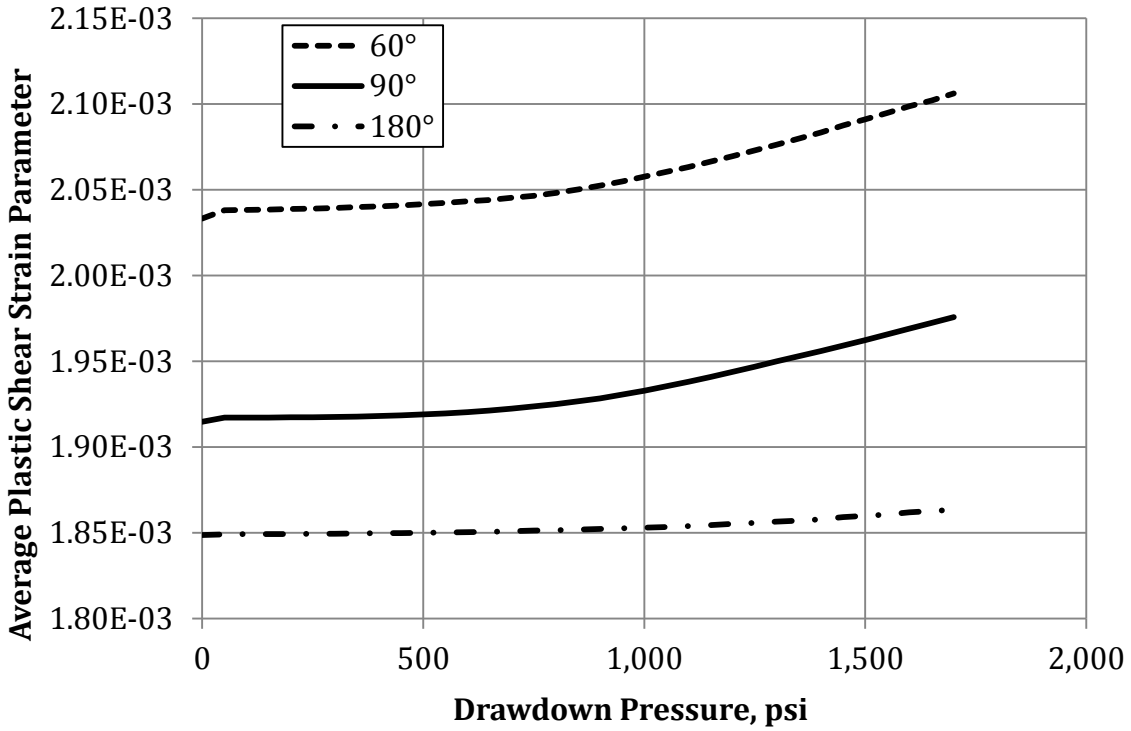

Figure 6.5: Development of plastic shear strain as a function of drawdown pressure for different perforation phasing angles.

6.1.3.2 Effect of Shot Density

Three cases with perforation densities of 4 SPF, 6 SPF, and 8 SPF were simulated. The results are shown in Figure 6.6.

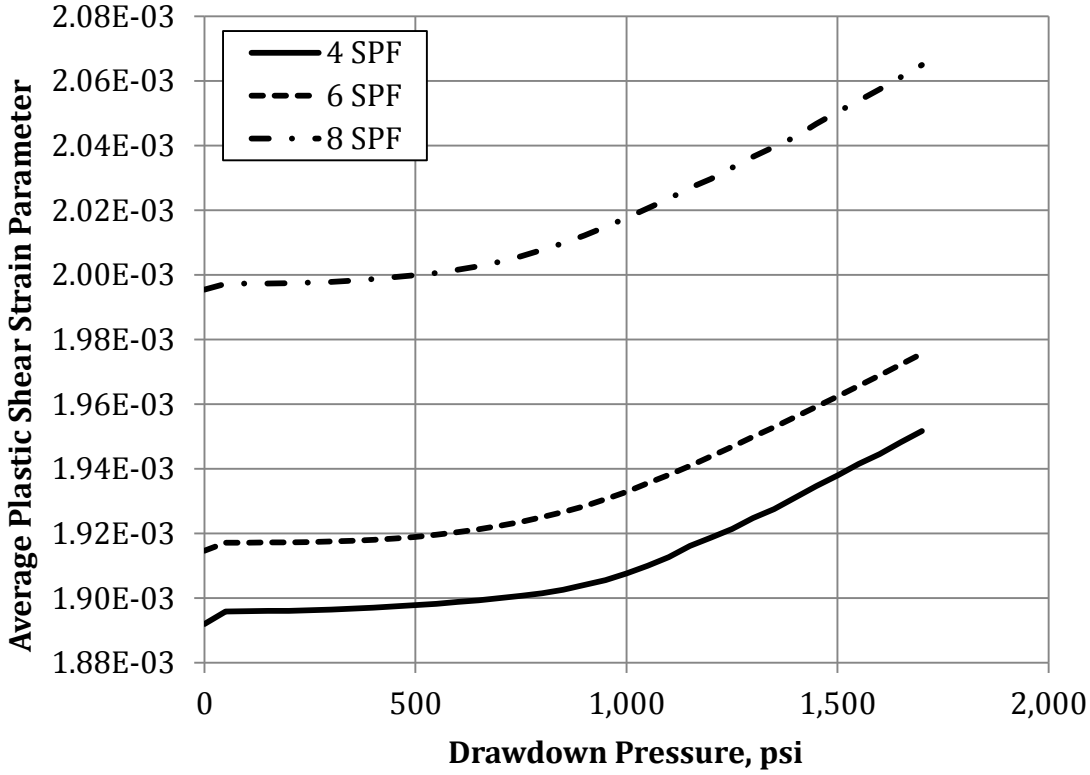

Figure 6.6: Development of plastic shear strain as a function of drawdown pressure for different perforation densities.

6.1.3.3 Effect of Wellbore Diameter

Three cases with wellbore diameter of 3-7/8 inches, 6-1/8 inches, and 8-1/2 inches were simulated. The results are shown in Figure 6.7.

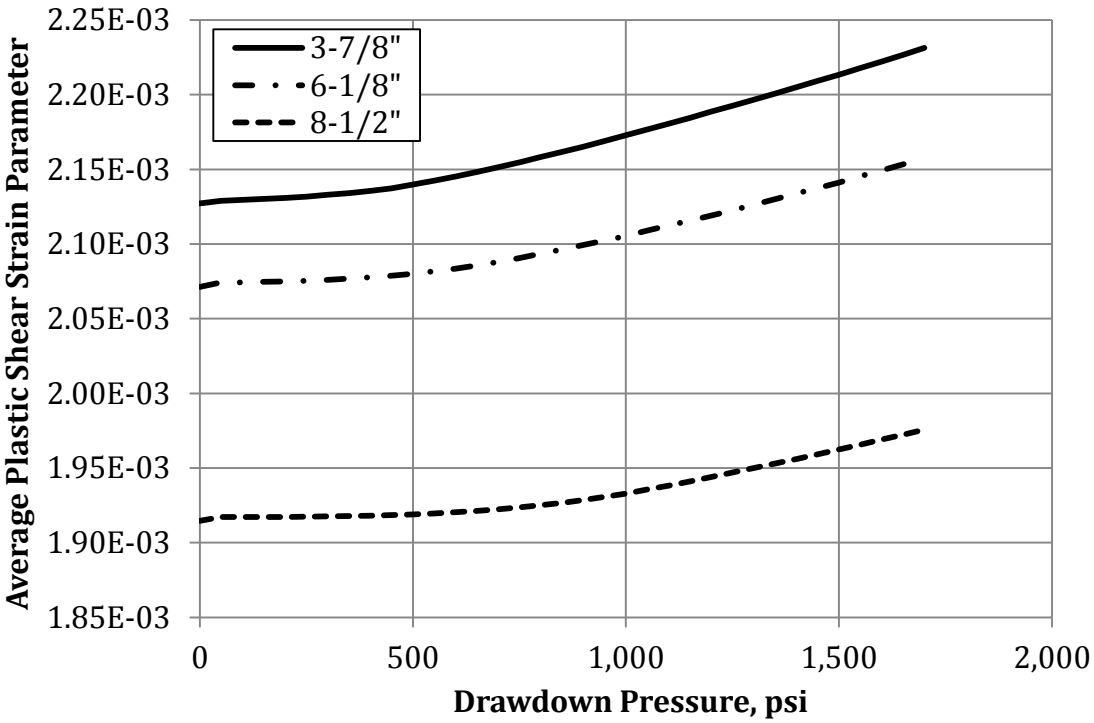

Figure 6.7: Development of plastic shear strain as a function of drawdown pressure for different wellbore diameters.

6.1.3.3 Mechanical Interference from Adjacent Perforations

Grid-blocks experiencing higher concentration of plastic flow are plotted in Figure 6.8 for both 6-1/8" and 8-1/2" wellbores at 90° and 6SPF. As shown in the graphs, the smaller wellbore experiences a higher degree of interlinking between the plastified zones.

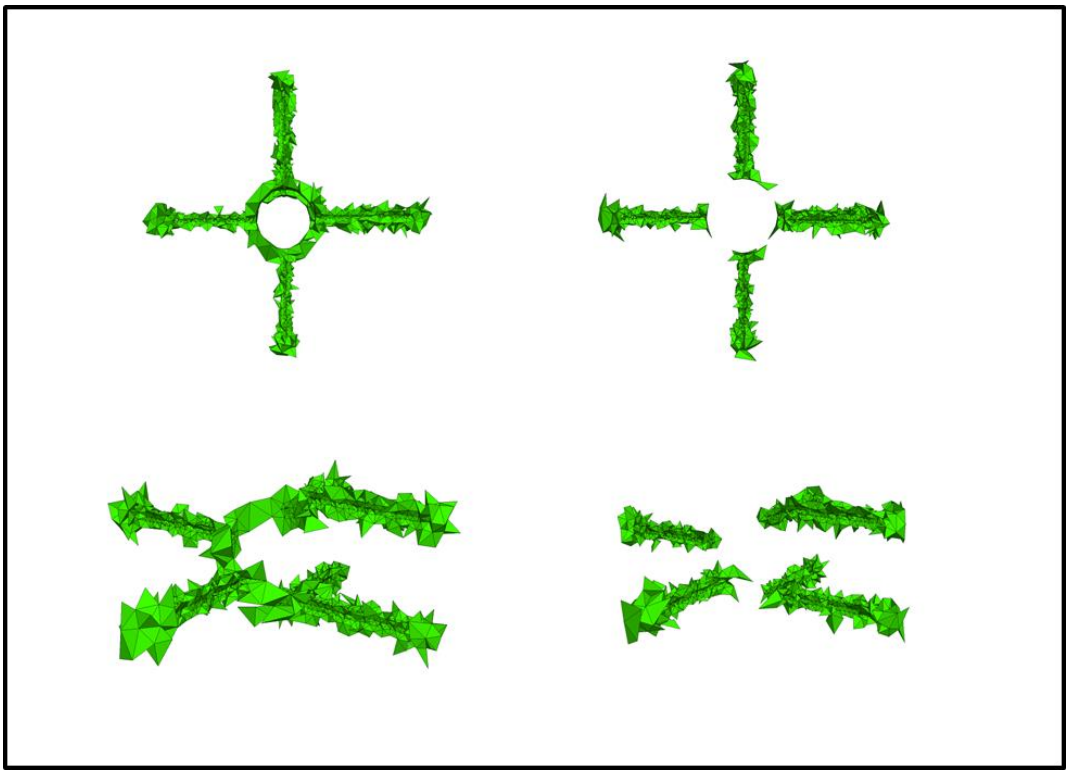

Figure 6.8: Concentration of plastic strain around the wellbore and perforation tunnel for 6-1/8" (left) and 8-1/2" (right) wellbores.

6.2 Discussion of Results

Results obtained from the simulation with the new model that was developed were generally in agreement with the studies reported in the literature. Both tensile and shear failure were encountered in the simulation runs as modes of failure, with the former being more prominent for the cases studied.

As shown in Figure 6.1, a vertical wellbore experiences considerably less sanding rate compared with the other wellbore configurations, in case the overburden stress is the maximum in-situ principal stress. Examples of this stress regime are encountered in many oil and gas basins around the world such as the

Gulf of Mexico and some of the tectonically relaxed regions of the North Sea. In addition, wells drilled in the direction of the maximum horizontal principal stress show higher sanding rate. In all cases, sand production stops at a certain drawdown pressure; this is a result of reaching the boundaries of the evaluation zone, in which no more sand is available in the grid to be produced. The amount of the produced sand prior to reaching the evaluation zone boundaries depends on the erosion pattern. Figure 6.9 shows an example pattern.

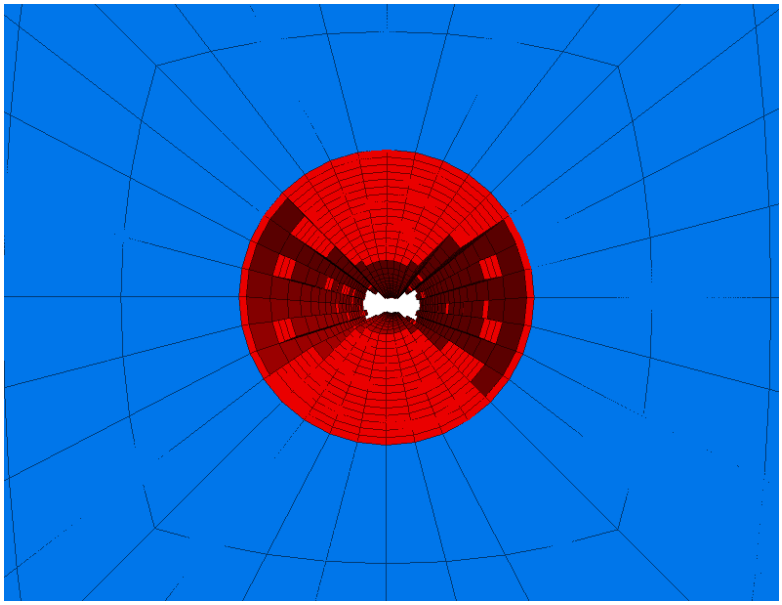

Figure 6.9: Sand erosion pattern in a horizontal wellbore where the boundaries of the evaluation zone are reached. (Direction of the max stress)

Figure 6.2 demonstrates the effect of reservoir depletion. Reduction in reservoir pressure leads to more sand production. However, wellbores with higher mechanical stability experience less sensitivity to changes in reservoir pressure as in the case of a vertical wellbore.

Studying sanding from open-holes can also provide an insight into sanding occurrence from perforation tunnels. Figure 6.10 shows the development of plastic shear strain around a horizontal wellbore tunnel. Perforating outside the plastified zone would result in more stable perforations. Similar results for have been reported by Morita and McLeod (1995) as shown in Figure 2.11.

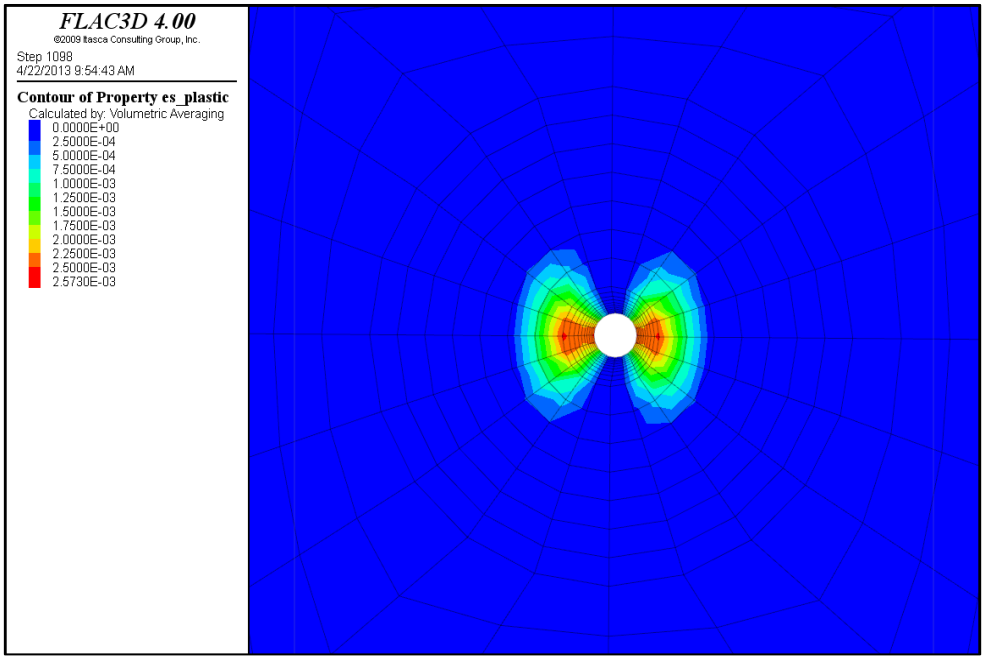

Figure 6.10: Development of plastic shear strain around a horizontal wellbore cavity, showing localized failure in the horizontal direction.

Sanding was simulated from perforation tunnels in a horizontal wellbore as shown in Figure 6.3. The figure shows that the critical drawdown pressure for a vertically-shot perforation is 500 psi higher than a horizontally-shot perforation. For a vertical wellbore, perforation orientation does not seem to have a significant impact on sanding. This outcome shows that oriented perforating is only important in the case of large stress anisotropy. Similar to the wellbore model, sanding starts

to level out at 300 kg; this is a result of reaching the boundaries of the evaluation zone.

For the multiple perforation runs, it is evident that more separation between perforations will generally lead to less plastic development and higher stability. Spacing between perforations is a function of shot density, phasing angle, and wellbore diameter. Following the study by Venkitaraman et al. (2000) discussed in Chapter 2, the spacing distances: L_1, L_2, and L_3 were calculated between the perforation openings along the wellbore wall for the different simulation runs as shown in Table 6.5. The peak strength ratio, defined as the ratio of the plastic shear strain intensity, γ^p, to the peak plastic shear strain intensity at the end of the hardening regime, γ_p^p, is calculated for each case at the end of simulation run.

$$R^p = \frac{\gamma^p}{\gamma_p^p} \tag{6.1}$$

In addition, the volumetric fluid flow rate, q, produced from the studied perforation was computed at 200 psi drawdown. The results for the flow rate are also shown in Table 6.5 in the units of barrels per day (bbl/d).

Table 6.5: The peak strength ratio and distances (in meters) between adjacent perforations for the different simulation runs

Run number	Wellbore diameter	Shot density	Phasing angle	L_1, m	L_2, m	L_3, m	R^p	q, bbl/d
1	8-1/2"	4 SPF	90°	0.320	0.294	0.188	65.1%	102.2
2	8-1/2"	6 SPF	90°	0.200	0.227	0.177	65.9%	91.9
3	8-1/2"	8 SPF	90°	0.160	0.208	0.170	68.8%	72.7
4	8-1/2"	6 SPF	60°	0.300	0.274	0.124	70.2%	83.5
5	8-1/2"	6 SPF	180°	0.100	0.343	0.343	62.1%	65.7
6	3-7/8"	6 SPF	90°	0.200	0.169	0.092	74.4%	80.8
7	6-1/8"	6 SPF	90°	0.200	0.194	0.133	71.9%	87.0

Based on these results, mechanical stability of multiple perforations appears to be more complex than initially anticipated; no direct relationship was observed between R^p and any of the spacing distances. Combinations of several mechanical, geometrical, and hydraulic factors all contribute in determining the stability of perforation tunnel. However, for a given wellbore diameter and shot density, the highest stability was established when two spacing distances were made equal (Run 5). However, it has the lowest production rate when compared with the runs with the same wellbore diameter and shot density (Runs 2 and 4).

Furthermore, inter-linking between plastified zones is also affected of the perforation spacing. Figure 6.8 shows that decreasing the distance between adjacent perforations by reducing the wellbore diameter resulted in a spatially continuous zone of concentrated plastic stain that surrounds the wellbore and the perforation tunnels.

It has been also observed that the transition to the softening regime results in an accelerated spread of failed zones leading to total collapse of the structure. In addition, softened zones exhibit higher sensitivity to changes in drawdown pressure.

6.3 CONCLUSION

Sand production is a complex process and many factors play a significant role in determining when sanding occurs and the rate of sand production. All these factors must be taken into consideration in order to design an optimum well completion.

Stability of wellbores and perforations in unconsolidated sands is greatly dependent on the post-yield mechanical behavior of the sand. Modeling the post-yield behavior of sand is accomplished by relating the cohesive strength, internal friction, dilation, and tensile strength to a hardening parameter that captures the history of the plastic strain.

Simulation results show that in areas where the overburden stress is the maximum in-situ stress, vertical wells will produce less sand. For horizontal wells, it is preferable to place the well in the direction of the minimum horizontal stress especially if large stress anisotropy exists.

When designing a perforated completion, several measures need to be taken. First, spacing between perforations should be sufficient to prevent inter-linking between the plastified zones. This measure can be accomplished through reducing the perforation density, higher phasing angle, or larger wellbores. Second, oriented perforations should be considered in the case of high stress anisotropy. This will both delay the onset of sand production and reduce its rate. If the overburden stress is the maximum in-situ stress, vertically oriented perforations are more stable in horizontal wellbores. Finally, avoiding the transition to the softening region throughout the operating life of well is recommended, if possible.

It is difficult to indicate a specific degree of stress anisotropy in which orienting the wellbore and perforation becomes advisable. However, based on the

formation mechanical and hydraulic properties, the developed model is capable of predicting if this completion strategy is advantageous. The mechanical behavior of perforated completions is a physically complicated process; advanced modeling techniques must be deployed to accurately design a completion with the least sanding risk.

The model presented in this thesis can be utilized to design a smart perforating strategy that will maximize the overall completion stability. If such a strategy is applied successfully, the need to install sand control equipment, such as sand screen or gravel packs, can be avoided or delayed to a later stage during the life of the well. Operating the well below the predicted critical drawdown pressure can also lead to similar results. Furthermore, sanding can be reduced to a rate that is safely managed at the surface. Even if sand control equipment is to be installed, proper perforation and wellbore placement leads to higher efficiency and operational longevity of the installed equipment.

References

1. Antheunis, D., Vriezen, P.B., Schipper, B.A., et al. 1976. Perforation Collapse: Failure of Perforated Friable Sandstones. Paper SPE 5750 presented at SPE European Spring Meeting, Amsterdam, The Netherlands, 8-9 April.

2. Behrmann, L.A., Willson, S.M., de Bree, Ph., et al. 1997. Field Implications from Full-Scale Sand Production Experiments. Paper SPE 38639 presented at the SPE Annual Technical Conference and Exhibition, San Antonio, Texas, 5-8 October.

3. Biot, M.A. 1941. General Theory of Three-Dimensional Consolidation. *Journal of Applied Physics* **12** (2): 155-164.

4. Bradford, I.D.R. and Cook, J.M. 1994. A Semi-analytical Elastoplastic Model for Wellbore Stability with Applications to Sanding. Paper SPE 28070 presented at the Rock Mechanics in Petroleum Engineering Conference, Delft, The Netherlands, 29-31 August.

5. Bradley, W. B. 1979. Failure of Inclined Boreholes. *Journal of Energy Resources Technology* **101** (4): 232-239. ASME-78-Pet-44.

6. Bratli, R.K. and Risnes, R. 1981. Stability and Failure of Sand Arches. *Society of Petroleum Engineers Journal* **21** (2): 236-248. SPE-8427-PA.

7. Chin, L.Y. and Ramos, G.G. 2002. Predicting Volumetric Sand Production in Weak Reservoirs. Paper SPE 78169 presented at the SPE/ISRM Rock Mechanics Conference, Irving, Texas, 20-23 October.

8. Cleary, M.P., Melvan, J.J., and Kohlhaas, C.A. 1979. The Effect of Confining Stress and Fluid Properties on Arch Stability in Unconsolidated Sands. Paper SPE 8426 presented at the SPE Annual Technical Conference and Exhibition, Las Vegas, Nevada, 23-26 September.

9. Detournay, C. and Dzik, E. 2006. Nodal Mixed Discretization for Tetrahedral Elements. Paper 07-02 presented at the 4th International FLAC Symposium on Numerical Modeling in Geomechanics, Madrid, Spain, 29-31 May.

10. Detournay, C., Tan, C., and Wu, B. 2006. Modeling the Mechanism and Rate of Sand Production Using FLAC. Paper 08-10 presented at the 4th International FLAC Symposium on Numerical Modeling in Geomechanics, Madrid, Spain, 29-31 May.

11. Detournay, E. and Cheng, A.H.-D. 1993. Fundamentals of Poroelasticity. In *Comprehensive Rock Engineering: Principles, Practice, and Projects*, ed. J.A. Hudson, Volume 2, Chapter 5, 113-171. Oxford, United Kingdom: Pergamon Press.

12. Fjær, E., Cerasi, P., Li, L., et al. 2004. Modeling the Rate of Sand Production. Paper ARMA 04-588 presented at Gulf Rocks 2004, the 6th North America Rock Mechanics Symposium (NARMS), Houston, Texas, 5-9 June.

13. Fjær, E., Holt, R.M., Horsrud, P. et al. 2008. *Petroleum Related Rock Mechanics*, second edition. Amsterdam: Elsevier.

14. FLAC3D: Fast Lagrangian Analysis of Continua in 3 Dimensions. Version 4.0 User's Guide. 2009. Minneapolis, Minnesota.

15. Hall, C.D., Jr. and Harrisberger, W.H. 1970. Stability of Sand Arches: A Key to Sand Control. *Journal of Petroleum Technology* **22** (7): 821-829. SPE-2399-PA.

16. Hubbert, M.K. and Willis, D.G. 1957. Mechanics of Hydraulic Fracturing. *In Transactions of the Society of Petroleum Engineers*, Vol. 210, 153-168. SPE-686-G.

17. Jaeger, J.C. and Cook, N.G.W. 1979. *Fundamentals of Rock Mechanics*, third edition. London: Chapman and Hall.

18. Kim, A.S. and Sharma, M.M. 2012. A Predictive Model for Sand Production in Realistic Downhole Conditions. Paper ARMA 12-314 presented at the 46th U.S. Rock Mechanics/Geomechanics Symposium, Chicago, Illinois, 24–27 June.

19. Kim, A.S., Sharma, M.M., and Fitzpatrick, H. 2011. A Predictive Model for Sand Production in Poorly Consolidated Sands. Paper IPTC 15087 presented at the International Petroleum Technology Conference, Bangkok, Thailand, 7-9 February.

20. Kim, S. H. 2010. A Predictive Model for Sand Production in Poorly Consolidated Sands. MS Thesis, The University of Texas at Austin, Austin, Texas (December 2010).

21. Kooijman, A.P., van den Hoek, P.J., de Bree, Ph., et al. 1996. Horizontal Wellbore Stability and Sand Production in Weakly Consolidated Sandstones. Paper SPE

36419 presented at the SPE Annual Technical Conference and Exhibition, Denver, Colorado, 6-9 October.

22. Koojiman, A.P., Hallek, P.M., de Bree, Ph., et al. 1992. Large-Scale Laboratory Sand Production Test. Paper SPE 24798 presented at the SPE Annual Technical Conference and Exhibition, Washington, D.C., 4-7 October.

23. Morita, N. and McLeod, H. 1995. Oriented Perforation to Prevent Casing Collapse for Highly Inclined Wells. *SPE Drilling and Completion* **10** (3): 139-145. SPE-28556-PA.

24. Morita, N., Whitfill, D.L., Fedde, O.P., et al. 1989. Parametric Study of Sand-Production Prediction: Analytical Approach. *SPE Production Engineering* **4** (1): 25-33. SPE-16990-PA.

25. Morita, N., Whitfill, D.L., Massie, I., et al. 1989. Realistic Sand-Production Prediction: Numerical Approach. *SPE Production Engineering* **4** (1): 15-24. SPE-16989-PA.

26. Nouri, A., Vaziri, H., Belhaj, H., et al. 2004. Sand Production Prediction: A New Set of Criteria for Modeling Based on Large-Scale Transient Experiments and Numerical Investigation. Paper SPE 90273 presented at the SPE Annual Technical Conference and Exhibition, Houston, Texas, 26-29 September.

27. Palmer, I.D., Higgs, N., Ispas, I., et al. 2006. Prediction of Sanding Using Oriented Perforations in a Deviated Well, and Validation in the Field. Paper SPE 98252

presented at the International Symposium and Exhibition on Formation Damage Control, Lafayette, Louisiana, 15-17 February.

28. Papamichos, E. and van den Hoek, P.J. 1995. Size Dependency of Castlegate and Berea Sandstone Hollow-Cylinder Strength on the Basis of Bifurcation Theory. Paper ARMA 95-0301 presented at the 35th U.S. Symposium on Rock Mechanics, Reno, Nevada, 5-7 June.

29. Papamichos, E., Vardoulakis, I., Tronvoll, J., et al. 2001. Volumetric Sand Production Model and Experiment. *International Journal for Numerical and Analytical Methods in Geomechanics* **25** (8): 789-808.

30. Papanastasiou, P. C. and Vardoulakis, I. G. 1992. Numerical Treatment of Progressive Localization in Relation to Borehole Stability. *International Journal for Numerical and Analytical Methods in Geomechanics* **16** (6): 389-424.

31. Rahman, K., Khaksar, A., and Kayes, T. 2010. An Integrated Geomechanical and Passive Sand-Control Approach to Minimizing Sanding Risk from Openhole and Cased-and-Perforated Wells. *SPE Drilling and Completion* **25** (2): 155-167. SPE-116633-PA.

32. Rahmati, H., Jafarpour, M., Azadbakht, S., et al. 2013. Review of Sand Production Prediction Models. *Journal of Petroleum Engineering* **2013**. Article 864981.

33. Risnes, R., Bratli, R. K., and Horsrud, P. 1982. Sand Stresses around a Wellbore. *Society of Petroleum Engineers Journal* **22** (6): 883-898. SPE-9650-PA.

34. Rösler, J., Harders, H., and BäKer, M. 2010. *Mechanical Behaviour of Engineering Materials: Metals, Ceramics, Polymers and Composites*. Berlin: Springer-Verlag.

35. Santarelli, F.J., Ouadfel, H., and Zundel, J.P. 1991. Optimizing the Completion Procedure to Minimize Sand Production Risk. Paper SPE 22797 presented at the SPE Annual Technical Conference and Exhibition, Dallas, Texas, 6-9 October.

36. Schön, J.H. 2004. Physical Properties of Rocks: Fundamentals and Principles of Petrophysics. In *Handbook of Geophysical Exploration: Seismic Exploration.* ed. K. Hilbig and S. Treitel, Volume 18. Oxford, United Kingdom: Elsevier.

37. Skjærstein, A., Stavropoulou, M., Vardoulakis, I., et al. 1997. Hydrodynamic Erosion: A Potential Mechanism of Sand Production in Weak Sandstones. *International Journal of Rock Mechanics and Mining Sciences* **34** (3-4): 292.e1-292.e18.

38. Stein, N. and Hilchie, D.W. 1972. Estimating the Maximum Production Rate Possible from Friable Sandstones without Using Sand Control. *Journal of Petroleum Technology* **24** (9): 1157-1160. SPE-3499-PA.

39. Sulbaran, A.L., Carbonell, R.S., and López-de-Cárdenas, J.E. 1999. Oriented Perforating for Sand Prevention. Paper SPE 57954 presented at the SPE European Formation Damage Conference, The Hague, The Netherlands, 31 May-1 June.

40. Tausch, G.H. and Corley, C.B. Jr. 1958. Sand Exclusion in Oil and Gas Wells. *Drilling and Production Practice* **1958**: 66-82. API-58-066.

41. Tippie, D.B. and Kohlhaas, C.A. 1973. Effects of Flow Rate on Stability of Unconsolidated Producing Sands. Paper SPE 4533 presented at the Fall Meeting of the Society of Petroleum Engineers of AIME, Las Vegas, Nevada, 30 September-3 October.

42. Tixier, M.P., Loveless, G.W., and Anderson, R.A. 1975. Estimation of Formation Strength from the Mechanical-Properties Log. . *Journal of Petroleum Technology* **27** (3): 283-293. SPE-4532-PA.

43. Tronvoll, J., Eek, A., Larsen, I., et al. 2004. The Effect of Oriented Perforations as a Sand-Control Method: A Field Case Study from the Varg Field, North Sea. Paper SPE 86470 presented at the SPE International Symposium and Exhibition on Formation Damage Control, Lafayette, Louisiana, 18-20 February.

44. van den Hoek, P.J., Hertogh, G.M.M., Kooijman, A.P., et al. 1996. A New Concept of Sand Production Prediction: Theory and Laboratory Experiments. Paper SPE 36418 presented at the SPE Annual Technical Conference and Exhibition, Denver, Colorado, 6-9 October.

45. Vardoulakis, I. and Sulem, J. 1995. *Bifurcation Analysis in Geomechanics*. Glasgow, United Kingdom: Chapman & Hall.

46. Vardoulakis, I., Stavropoulou, M., and Papanastasiou, P. 1996. Hydro-Mechanical Aspects of the Sand Production Problem. *Transport in Porous Media* **22** (2): 225-244.

47. Vaziri, H., Barree, B., Xiao, Y., et al. 2002. What is the Magic of Water in Producing Sand?. Paper SPE 77683 presented at SPE Annual Technical Conference and Exhibition, San Antonio, Texas, 29 September-2 October.

48. Veeken, C.A.M., Davies, D.R., Kenter, C.J., et al. 1991. Sand Production Prediction Review: Developing an Integrated Approach. Paper SPE 22792 presented at the SPE Annual Technical Conference and Exhibition, Dallas, Texas, 6-9 October.

49. Venkitaraman, A., Behrmann, L.A., and Chow, C.V. 2000. Perforating Requirements for Sand Control. Paper SPE 65187 presented at the SPE European Petroleum Conference, Paris, France, 24-25 October.

50. Vermeer, P.A. and de Borst, R. 1984. Non-associated Plasticity for Soils, Concrete and Rock. *HERON* **29** (3): 1-64.

51. Vriezen, P.B., Spijker, A., and van der Vlis, A.C. 1975. Erosion of Perforation Tunnels in Gas Wells. Paper SPE 5661 presented at the Fall Meeting of the Society of Petroleum Engineers of AIME, Dallas, Texas, 28 September-1 October.

52. Walton, I.C., Atwood, D.C., Halleck, P.M., et al. 2001. Perforating Unconsolidated Sands: An Experimental and Theoretical Investigation. Paper SPE 71458

presented at the SPE Annual Technical Conference and Exhibition, New Orleans, Louisiana, 30 September-3 October.

53. Wan, R.G., Wang, J., and Liu, Y.N. 2003. Prediction of Volumetric Sand Production Using a Coupled Geomechanics-Hydrodynamic Erosion Model. Petroleum Society of Canada paper 2003-200 presented at the Canadian International Petroleum Conference, Calgary, Alberta, 10-12 June.

54. Zoback, M. D. 2010. *Reservoir Geomechanics*. Cambridge: Cambridge University Press.